Simultaneous liquid flow and drying on rotating cylinders

Chance Parrish and Satish Kumar*
Department of Chemical Engineering and Materials Science, University of Minnesota, Minneapolis, Minnesota 55455, USA

(Received 16 August 2019; accepted 4 February 2020; published 4 March 2020)

The coating and drying of nonflat discrete objects is a key manufacturing step for a wide variety of products. Flow of a thin nonvolatile liquid film on the outside of a rotating cylinder is commonly used as a model problem to study the coating of discrete objects. However, the behavior of a volatile particle-laden coating remains an important open problem. In this work we use lubrication theory to study the evolution of a liquid film laden with colloidal particles in the presence of solvent evaporation. Two coupled evolution equations describing variations in coating thickness and composition as a function of time and the angular coordinate are solved numerically. In the limit of a rapidly rotating cylinder, gravitational effects are negligible and linear stability analysis and nonlinear simulations demonstrate that nonuniform drying at higher drying rates may cause thickness and composition disturbances to regrow after initially decaying. When gravitational effects are significant, poor liquid redistribution at lower rotation rates and higher drying rates leads to less uniform coatings. Colloidal particles hinder liquid redistribution at high concentrations by increasing the viscosity, but help prevent rupture of the coating at more moderate concentrations. A parametric study reveals that both thickness and composition variations are minimized at high rotation rate, low drying rate, and moderate initial particle concentration.

DOI: 10.1103/PhysRevFluids.5.034001

I. INTRODUCTION

The coating and drying of nonflat discrete objects is an essential step in manufacturing a wide variety of products such as medical devices and endoprostheses [1–4], dip-molded food and polymer products [5–7], and rotationally molded hollow plastic objects [8,9]. Drug-eluting and friction-reducing coatings may be applied to medical devices, such as stents and catheters, to prevent rejection by the body or increase the ease of use [1–4]. Molding processes bear many similarities to these coating processes; a coating is applied to a rotating mold, solidified, and then stripped from the mold to yield the final product, e.g., fuel tanks and bins [5–9].

Gravity can drive flows that cause liquid to collect into droplets and fingers, resulting in coating nonuniformities. Uniform coatings are often desired, and coating defects such as thickness and composition variations may negatively impact coating functions [10]. After a liquid coating is applied, the solvent must be removed, and this drying step can affect liquid distribution on the object to be coated. The effect of drying on the coating of nonflat discrete objects remains an important open problem.

An extensive body of work has examined the flow of nonvolatile liquids on rotating discrete objects, as summarized by Evans *et al.* [11,12]. Rotation of liquid-coated nonflat objects is often used to control distribution of liquid on a substrate. Moderate rotation rates may be used to prevent

*Corresponding author: kumar030@umn.edu

the formation of droplets on the underside of the objects, while higher rotation rates may be used to shed excess liquid [2]. Liquid flows on the outside of rotating cylinders are the simplest and most extensively investigated example of flows on the outside of nonflat rotating objects.

Moffatt [13] investigated flows of thin liquid films on rotating cylinders in the absence of surface tension by invoking the lubrication approximation and neglecting liquid flow along the cylinder axis. By examining the balance between viscous and gravitational forces, Moffatt [13] determined that a coating of mean thickness H may be supported on a cylinder by a minimum rotation rate

$$\Omega_c = \left(\frac{2\pi}{4.443}\right)^2 \left(\frac{H}{R}\right)^2 \frac{\rho g R}{\mu}, \tag{1.1}$$

where R is the cylinder radius, ρ is the liquid density, μ is the liquid viscosity, g is the gravitational acceleration, and Ω_c is the critical rotation rate. Above the critical rotation rate Ω_c, the mass flux Q around the cylinder is constant, and a steady-state coating may be obtained that is thicker on the upward-moving side of the cylinder and thinner on the downward-moving side. Good agreement between the observed critical rotation rate and that predicted from Eq. (1.1) has been demonstrated through flow-visualization experiments [14,15].

Experimental observations by Moffatt [13] revealed the formation of a rotating lobe of liquid that revolved around the cylinder for $\Omega > \Omega_c$. Subsequent numerical analyses [11,16] captured the behavior of the rotating lobe by incorporating surface tension into the model of Moffatt [13]. Pukhnachev [17] reasoned that the addition of surface tension may smooth out shocks and discontinuities. Hinch and Kelmanson [16] demonstrated that the decay rate of the rotating lobe is strongly proportional to the film thickness and inversely proportional to the viscosity.

Hynes [18], Evans *et al.* [11], and Karabut [19] showed that steady states for $\Omega < \Omega_c$ may be obtained by including the effects of surface tension and also explored the effects of centrifugal forces on the coating. Additionally, Hynes examined the stability of these steady states to angular and axial perturbations. The nonaxisymmetric shape of the coating in the presence of gravity imparts additional surface-tension and centrifugal forces that stabilize the free surface [18,20]. Lopes *et al.* [21] added to this body of work by exploring the formation of unstable steady states where liquid will likely be shed from the cylinder. Kelmanson [22] examined the effects of centrifugal forces on the evolution of the coating, showing the existence of unstable oscillatory solutions at higher rotation rates.

Investigations of the effects of drying on coating flows on nonflat rotating discrete objects are lacking. An extensive set of investigations has examined the evolution of volatile single- and multicomponent coatings on flat and patterned planar substrates, as reviewed in Refs. [23,24]. These investigations have shed light on the dynamics of volatile thin liquid films subjected to a variety of forces, including thermal- and surfactant-induced Marangoni forces [25–31] and intermolecular forces between the coating and substrate that may lead to film rupture [32]. Of these studies, flows of volatile and nonvolatile liquids on planar inclined substrates [26,33–35] are the closest analog to the rotating-cylinder problem, as the effects of gravity on the evolution of the coating are taken into account.

The present work extends the model of Evans *et al.* [11] to study the flow of a volatile coating laden with colloidal particles on a rotating cylinder. Colloidal suspensions are often used as coating liquids and are an important model system to explore. We consider cases where gravitational effects are negligible and significant, as we are interested in developing fundamental understanding and both cases are relevant for practical applications. In the absence of gravity, drying is incorporated into the linear analyses of Refs. [11,18] to understand its effects on the evolution of thickness and composition variations. In the presence of gravity, we study the evolution of a drying coating under conditions initially below the critical load criterion [Eq. (1.1)] where a hanging droplet should form on the underside of the cylinder. We observe a transition from a hanging droplet to a rotating lobe as a result of mass losses and viscosity increases during drying and we characterize how this transition influences coating uniformity.

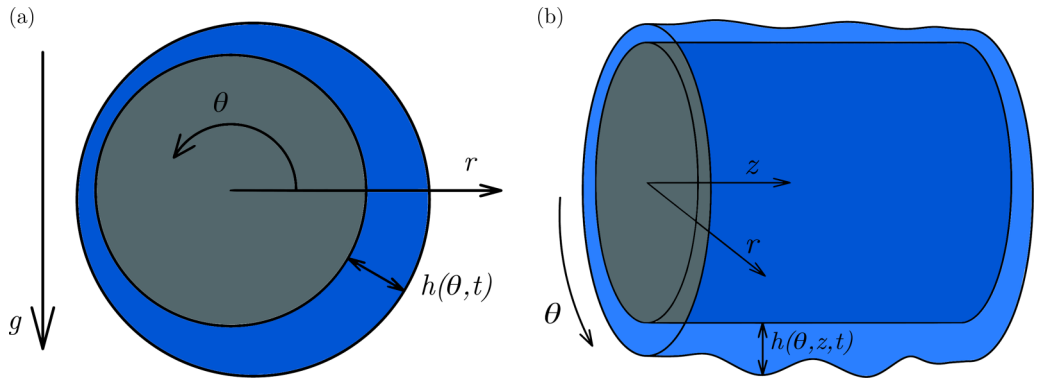

FIG. 1. Model geometry.

In Sec. II we present a lubrication-theory-based model to describe the evolution of a volatile particle-laden coating on a two-dimensional cross section of a rotating cylinder, where flows and variations in the axial direction have been neglected. We start with the limiting case of a volatile coating in the absence of gravity in Sec. III and then move on to the case including gravity in Sec. IV. A summary and conclusions are provided in Sec. V.

II. MATHEMATICAL MODEL

We consider the behavior of a drying particle-laden liquid film that fully wets a circular cylinder of radius R rotating counterclockwise at angular speed Ω. The liquid film consists of a stable suspension of colloidal particles within a volatile Newtonian solvent. Mass concentrations of the particles and solvent are defined as c_p and c_s, respectively. The densities of the colloidal particles are considered identical to the solvent density so that the mixture density is constant and the influence of particle adsorption to the cylinder surface or liquid-air interface is neglected. A description of the mixture viscosity is provided in Sec. II A.

The problem is defined in a cylindrical coordinate system (r, θ, z) (Fig. 1), where $h(\theta, z, t)$ represents the thickness of the liquid film with respect to the cylinder radius. For convenience, a new radial coordinate $y = r - R$ is defined on the interval $0 \leqslant y \leqslant h$. Within this region, we describe the liquid velocity as

$$\boldsymbol{u} = u_r \boldsymbol{e_r} + (\Omega R + u_\theta)\boldsymbol{e_\theta} + u_z \boldsymbol{e_z}, \tag{2.1}$$

where the angular component of the velocity has been decomposed into two parts: solid-body rotation and the deviation therefrom [36]. At the cylinder surface, the liquid temperature is identical to the cylinder temperature T_c, which is above the saturation temperature of the solvent. At the liquid-air interface, the film is in contact with a saturated vapor of the solvent, held at its saturation temperature T_{sat}. Drying of the liquid film will be described using the one-sided model of Ref. [32], with more details provided in Sec. II A.

A. Governing equations

The equations governing mass and momentum conservation for a constant density, variable viscosity liquid are

$$\nabla \cdot \boldsymbol{u} = 0, \tag{2.2}$$

$$\rho\left(\frac{\partial \boldsymbol{u}}{\partial t} + \boldsymbol{u} \cdot \nabla \boldsymbol{u}\right) = -\nabla p + \nabla \cdot \boldsymbol{\tau} + \rho \boldsymbol{g}, \tag{2.3}$$

where $\boldsymbol{g} = -g\sin\theta\boldsymbol{e_r} - \cos\theta\boldsymbol{e_\theta}$ is the gravitational acceleration in a fixed reference frame, p is the liquid pressure, and $\boldsymbol{\tau} = \mu(\phi)[\nabla\boldsymbol{u} + (\nabla\boldsymbol{u})^T]$ is the viscous stress tensor. We model the viscosity $\mu(\phi)$ using the relationship derived in Refs. [37,38] in the absence of shear thinning,

$$\mu(\phi) = \mu_s\left(1 - \frac{\phi}{0.64}\right)^{-2}. \tag{2.4}$$

Here μ_s is the viscosity of the coating liquid in the absence of colloidal particles and ϕ is the particle volume fraction given by c_p/ρ. In Eq. (2.4) it is assumed that the colloidal particles are rigid spheres whose maximum random packing fraction is $\phi_m = 0.64$. Note that as ϕ approaches ϕ_m, the viscosity rapidly diverges and the coating effectively solidifies. For simplicity, we neglect thermoviscous effects [39,40].

Evolution of the liquid temperature and composition is described by a set of convection-diffusion equations

$$\frac{\partial T}{\partial t} + \boldsymbol{u}\cdot\nabla T = \alpha\nabla^2 T, \tag{2.5}$$

$$\frac{\partial \phi}{\partial t} + \boldsymbol{u}\cdot\nabla\phi = D\nabla^2\phi, \tag{2.6}$$

where α, the liquid thermal diffusivity, and D, the diffusivity of colloidal particles, are taken to be constants. Although other authors have included the dependence of the particle diffusivity D on the concentration, this dependence was not found to substantially alter the key results in related problems [33]. In the course of the present work we briefly examined the evolution of a coating where particle diffusivity depends on composition. Compared to the case of a constant diffusivity, only minor quantitative changes in the results are observed. Since no qualitative changes occur, we choose to neglect the dependence of D on ϕ in this paper.

On the cylinder surface, we fix the liquid temperature, apply a no-flux boundary condition for colloidal particle transport, and apply no-slip and no-penetration boundary conditions for the liquid velocities,

$$T = T_c, \tag{2.7}$$

$$\frac{1}{r}\frac{\partial}{\partial y}\left(r\frac{\partial\phi}{\partial y}\right) = 0, \tag{2.8}$$

$$u_r = u_\theta = u_z = 0. \tag{2.9}$$

At the liquid-air interface $y = h$, we apply interfacial balances for total mass, normal stress, tangential stress, particle mass, and energy, respectively [32,41,42],

$$(\boldsymbol{u}^l - \boldsymbol{u}^I)\cdot\boldsymbol{n} = (\boldsymbol{u}^v - \boldsymbol{u}^I)\cdot\boldsymbol{n} = J, \tag{2.10}$$

$$\frac{J}{\rho^l}(\boldsymbol{u}^l - \boldsymbol{u}^v)\cdot\boldsymbol{n} + p^l - [\boldsymbol{n}\cdot\boldsymbol{\tau}\cdot\boldsymbol{n}]^l - p^v + [\boldsymbol{n}\cdot\boldsymbol{\tau}\cdot\boldsymbol{n}]^v = \sigma\nabla\cdot\boldsymbol{n}, \tag{2.11}$$

$$-[\boldsymbol{n}\cdot\boldsymbol{\tau}\cdot\boldsymbol{t_i}]^l + [\boldsymbol{n}\cdot\boldsymbol{\tau}\cdot\boldsymbol{t_i}]^v = -\nabla_s\sigma\cdot\boldsymbol{t_i} \quad (i = \theta, z), \tag{2.12}$$

$$\frac{\phi J}{\rho^l} - D\,\nabla\phi\cdot\boldsymbol{n} = 0, \tag{2.13}$$

$$J\left[\Delta H_v + \frac{1}{2}\left(\frac{J}{\rho^l}\right)^2 - \left(\frac{J}{\rho^v}\right)^2\right] = -k_{\text{th}}^l\boldsymbol{n}\cdot\nabla T^l + k_{\text{th}}^v\boldsymbol{n}\cdot\nabla T^v, \tag{2.14}$$

where the superscripts l, v, and I denote, respectively, liquid, vapor, and interface quantities. The scalars k_{th}, σ, J, and ΔH_v are the thermal conductivity, surface tension, evaporative mass flux, and latent heat of evaporation, respectively. The vectors $\boldsymbol{n}$ and $\boldsymbol{t_i}$ are the outward unit normal vector and

the tangent vectors in the i direction, defined as

$$\boldsymbol{n} = \frac{\nabla F}{|\nabla F|}, \tag{2.15}$$

$$\boldsymbol{t}_\theta = \left[\frac{1}{r}\frac{\partial h}{\partial \theta}\boldsymbol{e_r} + \boldsymbol{e_\theta}\right]\left[1 + \left(\frac{1}{r}\frac{\partial h}{\partial \theta}\right)^2\right]^{-1/2}, \tag{2.16}$$

$$\boldsymbol{t}_z = \left[\frac{\partial h}{\partial z}\boldsymbol{e_r} + \boldsymbol{e_z}\right]\left[1 + \left(\frac{\partial h}{\partial z}\right)^2\right]^{-1/2}, \tag{2.17}$$

where $F(r, \theta, z, t)=z - h(\theta, z, t)=0$ is the function defining the free surface. In Eqs. (2.10)–(2.14), the evaporative mass flux J appears.

We model the evaporative mass flux by assuming that exchange of solvent from liquid to vapor is slower than diffusion of solvent vapor away from the interface, an important component of the one-sided model [32],

$$KJ = T^I - T_{\text{sat}} = T^l(y = h, \theta, z, t) - T_{\text{sat}}, \tag{2.18}$$

$$K = \left(\frac{T_{\text{sat}}^{3/2}}{\alpha \rho^v \Delta H_v}\right)\left(\frac{2\pi R_{\text{gas}}}{M_w}\right)^{1/2}. \tag{2.19}$$

It is assumed that the coating liquid, with interfacial temperature $T^I = T^l(y = h, \theta, z, t)$, is in contact with its corresponding saturated vapor, with temperature T_{sat}. The interfacial temperature has been elevated above T_{sat} by heating the cylinder surface, driving evaporation. Equation (2.18) is effectively a mass-transfer-coefficient model for the mass flux, where the mass transfer coefficient K^{-1} is dependent on the saturation temperature T_{sat}, the ideal gas constant R_{gas}, the liquid molecular weight M_w, and the accommodation coefficient α. The latter quantity represents the fraction of molecules that are exchanged between phases upon collision with the liquid-air interface.

The one-sided model applies to experimental conditions where a superheated liquid is in contact with its corresponding saturated vapor [32,43] and where transport of mass across the liquid-vapor interface is the rate-limiting step. Predictions of the one-sided model for evaporating water droplets agree well with experiments performed under these conditions [43]. An alternative approach to describe drying is the diffusion-limited model [44]. In this model, the rate-limiting step is taken to be diffusion of the volatile species through an unsaturated vapor, which drives a flux of the volatile species from the liquid to the vapor phase. Although a diffusion-limited model of evaporation may also be applied, it becomes necessary to model diffusion in the vapor phase.

B. Scaling and evolution equations

In many applications of interest, the characteristic thicknesses H of the liquid film is much smaller than the cylinder radius R. As a result, a small parameter $\epsilon = H/R \ll 1$ may be defined and the lubrication approximation may be invoked to simplify the governing equations. Following prior work [11,12,20,45], we introduce the dimensionless quantities (denoted by tildes)

$$\begin{gathered}(y, h) = H(\tilde{y}, \tilde{h}), \quad (r, z) = R(\tilde{r}, \tilde{z}), \quad t = \Upsilon \tilde{t}, \\ u_r = \epsilon U \tilde{u}, \quad u_\theta = U\tilde{v}, \quad u_z = U\tilde{w}, \\ p = P\tilde{p}, \quad T = \tilde{T}\Delta T + T_c, \quad \mu = \mu_s \tilde{\mu}.\end{gathered} \tag{2.20}$$

The characteristic speed $U = \rho g H^2/\mu_s$, characteristic pressure $P = \mu_s U/H$, and characteristic time $\Upsilon = R/U$ are representative of the gravitational drainage process. Additionally, the temperature difference $\Delta T = T_c - T_{\text{sat}}$ is a positive constant and provides the driving force for drying. We assume a constant surface tension in the present work to isolate the influence of solvent removal. Additional calculations we have performed that account for the variation of surface tension with

TABLE I. Dimensional values for various coating properties.

Constants	Order of magnitude
Viscosity μ_s (P)	0.1
Density ρ (g cm^{-3})	1
Surface tension σ (dyn cm^{-1})	72
Film thickness H (cm)	10^{-2}
Cylinder radius R (cm)	1–10
Particle diffusivity D (cm^2 s^{-1})	10^{-12}–10^{-11}
Drying rate (μm s^{-1})	10–100
Cylinder rotation rate Ω (rad s^{-1})	10
Latent heat of vaporization ΔH_v (J/g)	100–2000
Vapor density ρ^v (g cm^{-3})	10^{-3}
Saturation temperature T_{sat} (K)	323–373
Molecular weight M_w (g mol^{-1})	20–100
Accommodation coefficient α (unitless)	10^{-3}–1
Cylinder temperature T_c (K)	323–373
Liquid thermal conductivity k_{th} (W m^{-1} K^{-1})	0.1–1

temperature show that thermal Marangoni forces lead to only minor quantitative changes in the results. Order-of-magnitude estimates for select dimensional quantities in Eq. (2.20) are listed in Table I. Hereafter, we drop the tilde from dimensionless variables to simplify our notation.

Using the scaled parameters in Eq. (2.20), we simplify Eqs. (2.2)–(2.6) and the corresponding boundary conditions in Sec. II A according to the lubrication approximation [11,12,20,45], the one-sided model [32], and the rapid-vertical-diffusion approximation [46]. In the rapid-vertical-diffusion approximation, the particle concentration ϕ is defined as

$$\phi(y,\theta,t) = \bar{\phi}(\theta,t) + \epsilon^2 \text{Pe}\,\tilde{\phi}(y,\theta,t), \tag{2.21}$$

where $\bar{\phi}$ is the depth-average concentration, Pe is a Péclet number defined in Table II, and $\tilde{\phi}$ is the vertical fluctuation in particle concentration. The integral of the vertical fluctuation through the coating depth y is assumed to be zero and its magnitude ϵ^2Pe is assumed to be small. These simplifications result in a set of coupled evolution equations for the film thickness and depth-average particle volume fraction, and one quasisteady expression for the interfacial temperature.

TABLE II. Dimensionless parameters and typical values.

Parameter	Definition	Physical meaning	Typical value
M	$\mu_s/\rho\sqrt{gR^3}$	$\dfrac{\text{viscous forces}}{\text{gravitational forces}}$	$O(10^{-3})$
W	$\Omega/\sqrt{g/R}$	$\dfrac{\text{rotational forces}}{\text{gravitational forces}}$	$O(10^{-3}$–$10^{-2})$
Bo	$\rho g R^2/\sigma$	$\dfrac{\text{gravitational forces}}{\text{surface-tension forces}}$	$O(10$–$100)$
E	$\Delta T v/K\rho g R^2$	$\dfrac{\text{drying velocity}}{\text{gravitational velocity}}$	$O(10^{-6}$–$10^{-5})$
Bi	$\Delta H_v R/K k_{\text{th}}$	$\dfrac{\text{evaporative heat transfer rate}}{\text{conduction rate}}$	$O(10^5$–$10^6)$
Pe	$\rho g R^3/\mu_s D$	$\dfrac{\text{convective mass transfer rate}}{\text{diffusive mass transfer rate}}$	$O(10^6$–$10^7)$

In the present work we neglect any axial flows and variations to focus on how drying affects coating behavior around the cylinder circumference. We note that curvature of the coating in the axial direction will generate flows that affect coating curvature in the angular direction and this may lead to qualitatively different results. We rescale h and U in terms of R ($U = \rho g R^2/\mu_s$) as was done in Refs. [11,12] to obtain the leading-order evolution equations

$$(1+h)\frac{\partial h}{\partial t} = -E(1+h)T(h) - MW\frac{\partial}{\partial\theta}\left(h+\frac{h^2}{2}\right) + \frac{\partial}{\partial\theta}\left[\frac{\cos\theta}{\mu}\left(\frac{h^3}{3}+\frac{h^4}{2}\right)\right] - \frac{\partial}{\partial\theta}\left\{\frac{h^3}{3\mu}\left[(W^2-\sin\theta)\frac{\partial h}{\partial\theta} + \frac{1}{\mathrm{Bo}}\frac{\partial}{\partial\theta}\left(h+\frac{\partial^2 h}{\partial^2\theta}\right)\right]\right\}, \tag{2.22}$$

$$\left(h+\frac{h^2}{2}\right)\left(\frac{\partial\phi}{\partial t} + MW\frac{\partial\phi}{\partial\theta}\right) + h\tilde{v}\frac{\partial\phi}{\partial\theta} = \frac{1}{\mathrm{Pe}}\frac{\partial}{\partial\theta}\left(h\frac{\partial\phi}{\partial\theta}\right) + E(1+h)\phi T(h), \tag{2.23}$$

$$T = \frac{1}{1+\mathrm{Bi}(1+h)\ln(1+h)}, \tag{2.24}$$

where h is the rescaled thickness and ϕ is the depth-average particle concentration. For simplicity, the line over ϕ has been dropped. We note that while our original scaling allows for a systematic derivation using lubrication theory, rescaling using R allows all lengths to be measured in terms of a common scale. This is more convenient for presenting results and causes ϵ to appear only in the initial film thickness [11,12]. Table II provides definitions, physical meanings, and typical values of dimensionless parameters in Eqs. (2.22)–(2.24). The depth-average angular component of the velocity is given by

$$h\tilde{v} = -\frac{\cos\theta}{\mu}\left(\frac{h^3}{3}+\frac{h^4}{2}\right) + \frac{h^3}{3\mu}\left[\frac{\partial h}{\partial\theta}(W^2-\sin\theta) + \frac{1}{\mathrm{Bo}}\frac{\partial}{\partial\theta}\left(h+\frac{\partial^2 h}{\partial^2\theta}\right)\right]. \tag{2.25}$$

For a nonvolatile particle-free liquid ($E = 0$ and $\phi = 0$), Eq. (2.22) reduces to the evolution equation obtained in Ref. [11]. In the limit of $\mathrm{Bi} = 0$, heat transfer effects may be neglected and the coating temperature at the liquid-air interface is uniformly the cylinder temperature. In the limit of $\mathrm{Bi} \to \infty$, the coating temperature depends strongly on the film thickness as $h \to 0$. For all simulations presented here, we use one Biot number ($\mathrm{Bi} = 1.8\times10^6$) and one Bond number ($\mathrm{Bo} = 100$), which are representative of typical values. In Sec. IV we comment briefly on the effects of these parameters.

Given a fixed set of dimensionless parameters (Table II) and initial conditions, Eqs. (2.22) and (2.23) are solved using a partially implicit finite-difference scheme following Refs. [11,45]. The θ domain is discretized using a set of $n_\theta \geqslant 600$ evenly spaced nodes, with spacing given by $\Delta\theta = 2\pi/n_\theta$. The time domain is discretized using a fixed nondimensional time step $\Delta t \leqslant 50$, with the current time step being t^k and the next time step being t^{k+1}. The convective terms and drying terms, with respective coefficients MW and E, in Eqs. (2.22) and (2.23) are discretized in time using a trapezoid rule, where the average values at t^k and t^{k+1} are used to approximate their contribution to $\partial h/\partial t$. All other terms are discretized in the same manner as in Refs. [11,45].

Unless otherwise stated, uniform initial conditions for the film thickness $h(\theta, t=0) = \epsilon$ and particle volume fraction $\phi(\theta, t=0) = \phi_0$ are applied. We use a value of $\epsilon = 0.007$ in all simulations. Note that if the initial film thickness is too small, the film will evaporate away before significant flow occurs. If the initial film thickness is too large, disturbances to the film thickness will grow rapidly under the action of centrifugal forces or gravity, making it difficult to resolve the free-surface shape.

Simulations are ended when either of the following criteria is satisfied:

$$\min[h(\theta, t^{k+1})] \leqslant \epsilon/1000,$$
$$\max[\phi(\theta, t^{k+1})] \geqslant 0.635. \tag{2.26}$$

The time step at which the simulations are halted is henceforth called the dryout time, denoted by t_d. In simulations without particles ($\phi_0 = 0$), the minimum thickness criterion must be met. We refer to this mechanism as film rupture. If the maximum concentration is reached [cf. Eq. (2.4)], we refer to this dryout mechanism as solidification.

III. RAPIDLY ROTATING CYLINDER

Though our main interest is the behavior of a volatile coating in the presence of gravity, it is instructive to consider flow on a cylinder rotating so rapidly that gravitational effects are negligible. In this regime, different scales must be chosen for the governing equations. To do this, we neglect the gravitational terms in Eqs. (2.22) and (2.23) and rescale time and velocity using $\Upsilon = \mu_s R/\sigma$ and $U = \sigma/\mu_s$ [11,12,20,45], yielding the equations

$$(1+h)\frac{\partial h}{\partial t} = -\mathrm{Ca}_e(1+h)T(h) - \mathrm{Ca}_r\frac{\partial}{\partial\theta}\left(h+\frac{h^2}{2}\right) - \frac{\partial}{\partial\theta}\left\{\frac{h^3}{3\mu}\left[\mathrm{We}\frac{\partial h}{\partial\theta} + \frac{\partial}{\partial\theta}\left(h+\frac{\partial^2 h}{\partial^2\theta}\right)\right]\right\}, \tag{3.1}$$

$$\left(h+\frac{h^2}{2}\right)\left(\frac{\partial\phi}{\partial t} + \mathrm{Ca}_r\frac{\partial\phi}{\partial\theta}\right) + h\tilde{v}\frac{\partial\phi}{\partial\theta} = \frac{1}{\mathrm{Pe}_s}\frac{\partial}{\partial\theta}\left(h\frac{\partial\phi}{\partial\theta}\right) + \mathrm{Ca}_e(1+h)\phi T(h), \tag{3.2}$$

$$T = \frac{1}{1+\mathrm{Bi}(1+h)\ln(1+h)}, \tag{3.3}$$

where

$$h\tilde{v} = \frac{h^3}{3\mu}\left[\mathrm{We}\frac{\partial h}{\partial\theta} + \frac{\partial}{\partial\theta}\left(h+\frac{\partial^2 h}{\partial^2\theta}\right)\right] \tag{3.4}$$

and

$$\mathrm{Ca}_r = \frac{\mu_s\Omega R}{\sigma}, \quad \mathrm{Ca}_e = \frac{\mu_s\Delta T}{\sigma\rho K}, \quad \mathrm{We} = \frac{\rho\Omega^2R^3}{\sigma}, \quad \mathrm{Pe}_s = \frac{\sigma R}{\mu_s D}. \tag{3.5}$$

The parameters listed in Eq. (3.5) are a rotational capillary number Ca_r, a drying capillary number Ca_e, a Weber number We, and a Péclet number Pe_s, respectively. These dimensionless quantities set the timescales of solid-body rotation, drying, centrifugation, and particle diffusion relative to the capillary timescale.

A linear analysis will be conducted for Eqs. (3.1)–(3.4) in Sec. III A and compared to numerical solutions of Eqs. (3.1) and (3.2) in Sec. III B (particle-free liquid) and Sec. III C (particle-laden liquid).

A. Linear analysis

In the absence of gravitational forces, we study the fate of a spatially uniform coating whose thickness and composition have been perturbed by small-amplitude nonuniformities. Instead of making the frozen-base-state approximation [47], where the base state is assumed to evolve slowly compared to perturbations, we use a time-dependent base state to account for a base state that evolves on a similar timescale as the perturbations [30,48]. A linear stability analysis (LSA) is used to quantitatively examine the fate of these small perturbations for a given set of dimensionless parameters and initial conditions. Details of the LSA may be found in the Appendix.

The time-dependent base state consists of the solution to Eqs. (3.1) and (3.2) in the absence of spatial variations,

$$h_b(t) = \epsilon + \frac{\sqrt{2T(\epsilon)T_{hh} - T_h^2}\tan\left[-\frac{t\,\mathrm{Ca}_e}{2}\sqrt{2T(\epsilon)T_{hh} - T_h^2} - \cos^{-1}\left(\frac{-\sqrt{2T(\epsilon)T_{hh} - T_h^2}}{\sqrt{2T(\epsilon)T_{hh}}}\right)\right] - T_h}{T(\epsilon)}, \tag{3.6}$$

$$\phi_b(t) = \left(\epsilon + \frac{\epsilon^2}{2}\right)\phi_0\left(h_b + \frac{h_b^2}{2}\right)^{-1}. \tag{3.7}$$

Note that to obtain Eq. (3.6), a second-order Taylor-series expansion about $h_b(0) = \epsilon$ is applied. The initial conditions used are $h_b(0) = \epsilon$ and $\phi_b(0) = \phi_0$. The quantities T_h and T_{hh} are the first and second derivatives of $T(h)$ evaluated at the initial condition $h_b(0) = \epsilon$. The base state is perturbed by

$$h(\theta, t) = h_b(t) + \alpha h'(\theta, t),$$
$$\phi(\theta, t) = \phi_b(t) + \beta \phi'(\theta, t), \tag{3.8}$$

with small amplitudes α and β.

Equations (3.1) and (3.2) are linearized to yield

$$\frac{\partial h'}{\partial t} = -h'[T_h + (h_b - \epsilon)T_{hh}] - \mathrm{Ca}_r \frac{\partial h'}{\partial \theta} - \frac{h_b^3}{3\mu_b(t)(1+h_b)}\left((1+\mathrm{We})\frac{\partial^2 h'}{\partial^2 \theta} + \frac{\partial^4 h'}{\partial^4 \theta}\right), \tag{3.9}$$

$$\left(h_b + \frac{h_b^2}{2}\right)\frac{\partial \phi'}{\partial t} = -\phi' \frac{\partial}{\partial t}\left(h_b + \frac{h_b^2}{2}\right) - \mathrm{Ca}_r\left(h_b + \frac{h_b^2}{2}\right)\frac{\partial \phi'}{\partial \theta} + \frac{h_b}{\mathrm{Pe}_s}\frac{\partial^2 \phi'}{\partial^2 \theta}$$
$$+ \frac{\alpha}{\beta} h'\left[\mathrm{Ca}_e(1+h_b)(\phi_b)[T_h + T_{hh}(h_b - \epsilon)] - \frac{\partial}{\partial t}[\phi_b(1+h_b)]\right], \tag{3.10}$$

where μ_b is the time-dependent base-state viscosity

$$\mu_b(t) = \left(1 - \frac{\phi_b(t)}{0.64}\right)^{-2}. \tag{3.11}$$

We simplify Eq. (3.10) by dividing both sides of the equation by $\left(h_b + \frac{h_b^2}{2}\right)$,

$$\frac{\partial \phi'}{\partial t} = -p(t)\phi' - \mathrm{Ca}_r \frac{\partial \phi'}{\partial \theta} + \frac{q(t)}{\mathrm{Pe}_s}\frac{\partial^2 \phi'}{\partial^2 \theta} + \frac{\alpha}{\beta} r(t) h', \tag{3.12}$$

where $p(t)$, $q(t)$, and $r(t)$ are

$$p(t) = \frac{\partial}{\partial t}\left[\ln\left(h_b + \frac{h_b^2}{2}\right)\right], \tag{3.13}$$

$$q(t) = h_b\left(h_b + \frac{h_b^2}{2}\right)^{-1}, \tag{3.14}$$

$$r(t) = \left(h_b + \frac{h_b^2}{2}\right)^{-1}\left[\mathrm{Ca}_e(1+h_b)(\phi_b)[T_h + T_{hh}(h_b - \epsilon)] - \frac{\partial}{\partial t}[\phi_b(1+h_b)]\right]. \tag{3.15}$$

Solutions for h' and ϕ' may be obtained by separating each into

$$h'(\theta, t) = \bar{h}(t) e^{ik\theta}, \tag{3.16}$$

$$\phi'(\theta, t) = \bar{\phi}(t) e^{ik\theta}, \tag{3.17}$$

where $\bar{h}(t)$ and $\bar{\phi}(t)$ are the time-dependent amplitudes of each perturbation, with initial conditions $\bar{h}(0) = \bar{\phi}(0) = 1$. The wave number k must be an integer due to periodicity of $h(\theta, t)$ and $\phi(\theta, t)$ in the θ direction. Substitution of Eqs. (3.16) and (3.17) into Eqs. (3.9) and (3.12) yields a nonautonomous system of differential equations

$$\frac{1}{\bar{h}(t)}\frac{d\bar{h}(t)}{dt} = -\mathrm{Ca}_e\{T_h + T_{hh}[h_b(t) - \epsilon]\} - ik\,\mathrm{Ca}_r + \frac{h_b^3}{3\mu_b(t)(1+h_b)}[(1+\mathrm{We})k^2 - k^4], \tag{3.18}$$

$$\frac{d\bar{\phi}(t)}{dt} = -\bar{\phi}(t)\left(p(t) + ik\,\mathrm{Ca}_r - \frac{k^2 q(t)}{\mathrm{Pe}_s}\right) + \frac{\alpha}{\beta} r(t)\bar{h}(t). \tag{3.19}$$

From Eqs. (3.18) and (3.19), we expect that $\bar{h}(t)$ will evolve independently of $\bar{\phi}(t)$ at early times when linearization of Eqs. (3.1)–(3.4) is valid. However, evolution of $\bar{\phi}(t)$ is clearly coupled to $\bar{h}(t)$, and the effects of this coupling will be explored in Sec. III C. Solutions for $\bar{h}(t)$ and $\bar{\phi}(t)$ are obtained using the integrating-factor method (the Appendix) to yield

$$\bar{h}(t) = e^{\omega_h(t)}, \tag{3.20}$$

$$\bar{\phi}(t) = e^{-\omega_\phi(t)}\left(1 + \frac{\alpha}{\beta}\int_0^t r(\zeta)e^{\omega_\phi(\zeta)+\omega_h(\zeta)}d\zeta\right), \tag{3.21}$$

where

$$\omega_h(t) = -\int_0^t \left[\mathrm{Ca}_e\{T_h + T_{hh}[h_b(\zeta)-\epsilon]\} + ik\,\mathrm{Ca}_r - \frac{h_b^3}{3(1+h_b)}\left(1-\frac{\phi_b}{0.64}\right)^2[(1+\mathrm{We})k^2-k^4]\right]d\zeta, \tag{3.22}$$

$$\omega_\phi(t) = \int_0^t \left(p(\zeta) + \frac{k^2 q(\zeta)}{\mathrm{Pe}_s} + ik\,\mathrm{Ca}_r\right)d\zeta. \tag{3.23}$$

The real components of Eqs. (3.22) and (3.23) dictate the growth and decay of perturbations with respect to the time-varying base states h_b and ϕ_b. It is important to point out that the functions $\omega_h(t)$ and $\omega_\phi(t)$ are not perturbation growth rates, which have units of inverse time when dimensionalized. Instead, $\omega_h(t)$ and $\omega_\phi(t)$ represent unitless functions that dictate the growth and decay of perturbations. Because the amplification $\bar{h}(t)$ [Eq. (3.20)] is an exponential function of time, the eigenvalue

$$\lambda_h(t) = \frac{d\,\mathrm{Re}[\omega_h(t)]}{dt} = -\mathrm{Ca}_e\{T_h + T_{hh}[h_b(t)-\epsilon]\} + \frac{h_b^3}{3(1+h_b)}\left(1-\frac{\phi_b}{0.64}\right)^2[(1+\mathrm{We})k^2-k^4] \tag{3.24}$$

is a measure of the instantaneous growth rate of thickness perturbations, with dimensions of inverse time when redimensionalized.

It is difficult to obtain simple analytical expressions for Eqs. (3.20) and (3.21) due to the complicated time integrals that appear. Instead, Chebyshev approximations of Eqs. (3.20) and (3.21) are evaluated numerically using CHEBFUN [49]. Equations (3.20) and (3.21) can be evaluated for multiple sets of parameters in minutes, while simulations of Eqs. (3.1) and (3.2) may take minutes to an hour for a single set of parameters.

B. Particle-free liquid

Comparison of the LSA to numerical solutions of Eq. (3.1) in the absence of particles is done for validation and to highlight the effects of drying on the evolution of film-thickness perturbations. Simulations of Eq. (3.1) have been performed in a reference frame that rotates at angular speed Ca_r, which is accomplished by neglecting the solid-body rotation term (set $\mathrm{Ca}_r = 0$). We solve Eq. (3.1) with the initial condition

$$h(\theta, t=0) = \epsilon[1 + \alpha\sin(k\theta)], \tag{3.25}$$

where k is the wave number of the perturbation.

The eigenvalue $\lambda_h(t)$ is a convenient way to compare numerical results to the LSA,

$$\frac{\partial}{\partial t}[\ln(h_{\max} - h_{\min})] = \lambda_h(t) = -\mathrm{Ca}_e\{T_h + T_{hh}[h_b(t)-\epsilon]\} + \frac{h_b^3(t)}{3[1+h_b(t)]}[(1+\mathrm{We})k^2 - k^4], \tag{3.26}$$

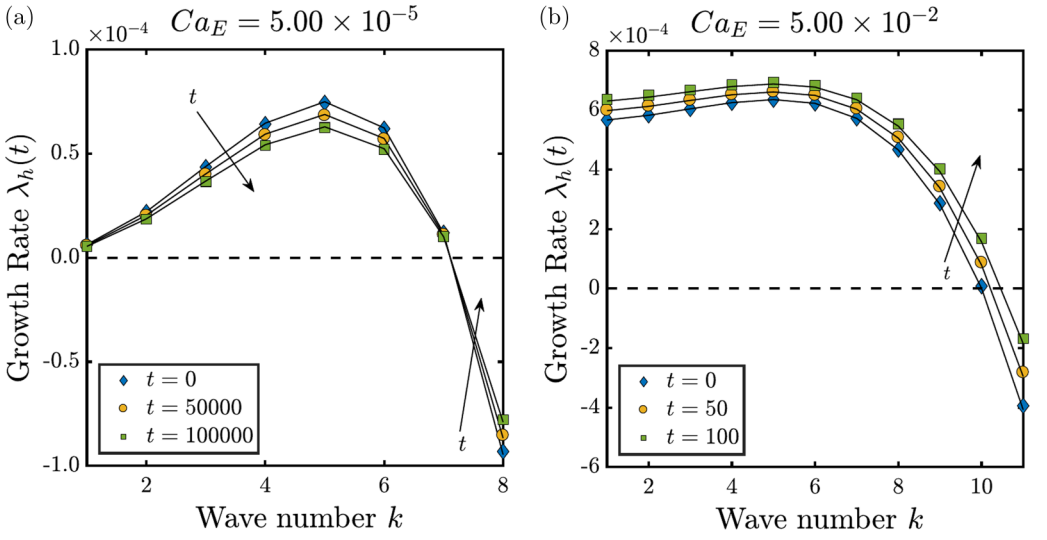

FIG. 2. Instantaneous growth rate of perturbations $\lambda_h(t)$ for a particle-free film at We = 50 for a range of wave numbers k and two drying rates: (a) $\mathrm{Ca}_e = 5.00\times10^{-5}$ and (b) $\mathrm{Ca}_e = 5.00\times10^{-2}$. Solid lines are LSA predictions and closed symbols are simulation results at times shown in the legends.

where $h_{\max}$ and $h_{\min}$ are the maximum and minimum thickness obtained from numerical results at a given time. The leftmost term in Eq. (3.26) is used to extract $\lambda_h(t)$ from the simulations. The rightmost term in Eq. (3.26) is Eq. (3.24) with $\phi_b = 0$.

The first contribution to the rightmost term in Eq. (3.26) is associated with drying and is anticipated to be destabilizing since $T_h < 0$ [cf. Eq. (3.3)]. If the film becomes thinner in places, the interfacial temperature increases, which in turn increases the evaporation rate and further thins the film. The second contribution to the rightmost term in Eq. (3.26) is identical to what would be obtained in the absence of drying. It reflects a competition between centrifugal forces, which are destabilizing, and surface-tension forces, which are stabilizing. Note that since the viscous forces are $\sim h_b^3$, lower instability growth rates would be expected as the film gets thinner.

In Fig. 2 we compare numerical results to the LSA for two representative cases. Excellent agreement is observed for both cases. In Fig. 2(a), where the drying rate is relatively low, the instantaneous growth rate decreases as time progresses, reflecting the increasing importance of viscous forces as the film gets thinner. In Fig. 2(b), where the drying rate is considerably higher, the instantaneous growth rate increases as time progresses, reflecting the destabilizing effect of the drying term in Eq. (3.26).

In Figs. 2(a) and 2(b) the fastest growing or most dangerous wave number remains fixed at $k = 5$ for both drying rates and for all times shown. As the wave number k must be an integer given the cylindrical geometry, the most dangerous wave number k_{crit} is expected to be the greatest integer less than $\tilde{k}$,

$$\tilde{k} = \sqrt{\frac{1+\mathrm{We}}{2}}, \tag{3.27}$$

where $\tilde{k}$ is obtained by solving $\partial\lambda_h(t)/\partial k = 0$. Note that Eq. (3.27) predicts that the most dangerous wave number is independent of drying rate (Ca_e), consistent with the results shown in Fig. 2.

To validate Eq. (3.27), additional simulations of Eq. (3.1) have been conducted using initial conditions consisting of a spatially uniform thickness perturbed by random noise of amplitude $\alpha\epsilon$,

$$h(\theta, t=0) = \epsilon\{1 + \alpha[R(\theta) - 0.5]\}, \tag{3.28}$$

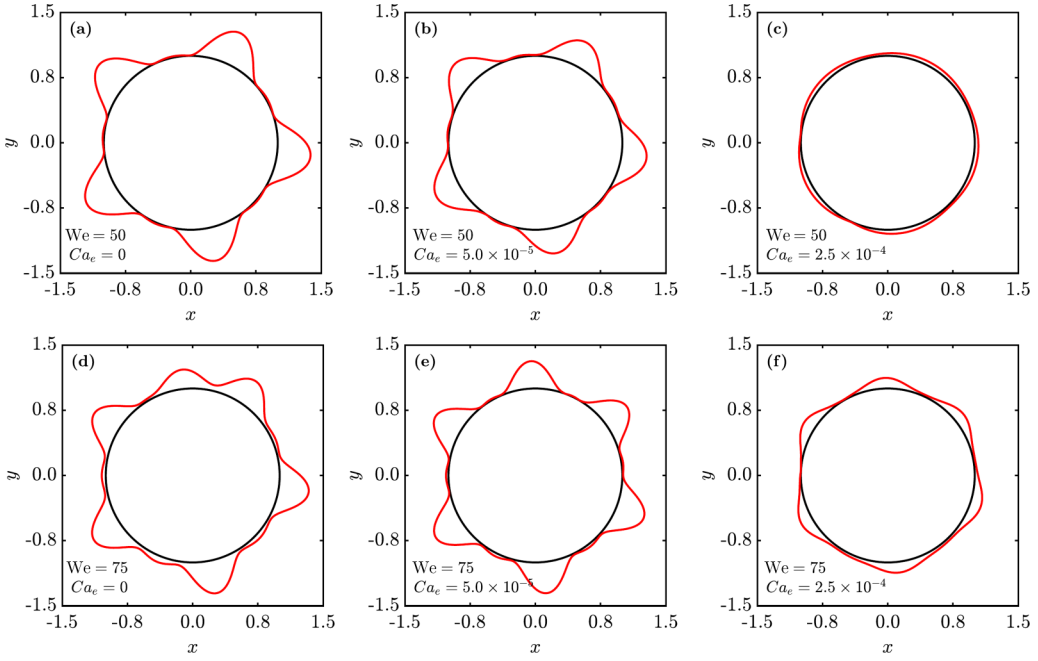

FIG. 3. Profiles of the liquid film obtained from simulation results, shown after droplet formation for $\mathrm{Ca}_e = 0$ and at $t = t_d$ for $\mathrm{Ca}_e \neq 0$. Drying rates and Weber numbers used in each simulation are shown in the same panel as the simulation results. Drying rates increase from left to right and Weber numbers increase from top to bottom. For We = 50 and We = 75, the expected number of droplets is $k_{\mathrm{crit}} = 5$ and $k_{\mathrm{crit}} = 6$, respectively.

where $R(\theta)$ is a set of pseudorandom numbers between 0 and 1. We set $\alpha = 1\times10^{-4}$ for all simulations in this paper. For $\mathrm{Ca}_e \neq 0$, simulations are carried out until t_d, the time at which $\min[h(\theta, t)] \leqslant \epsilon/1000$. For $\mathrm{Ca}_e = 0$, simulations are carried out until droplets have ceased growing.

Profiles of the liquid thickness are plotted at various times for two Weber numbers We and three drying rates Ca_e in Fig. 3. For $\mathrm{Ca}_e = 0$, thickness profiles are shown after droplet formation; for $\mathrm{Ca}_e \neq 0$, thickness profiles are shown at the dryout time $t = t_d$. At Weber numbers We = 50 [Figs. 3(a)–3(c)] and We = 75 [Figs. 3(d)–3(f)], five and six droplets form, respectively. These results are in good agreement with the values of k_{crit} calculated using Eq. (3.27) and the results shown in Fig. 2.

Another important feature of $\lambda_h(t)$ is the cutoff wave number k_c, where $\lambda_h(t)$ changes sign to signify a shift from growth to decay. In Fig. 2(a) the cutoff wave number is nearly constant and approximately equal to 7. In Fig. 2(b) an increase in the growth rates for all wave numbers occurs as time progresses. This increase in $\lambda_h(t)$ over time causes a change in the cutoff wave number, where k_c progresses from $k = 10$ toward $k = 11$.

An expression for the cutoff wave number may be obtained by solving $\lambda_h(t) = 0$,

$$k_c(t) = \left(\frac{(1 + \mathrm{We}) + \sqrt{(1 + \mathrm{We})^2 - 12\,\mathrm{Ca}_e[T_h + T_{hh}(h_b - \epsilon)](1 + h_b)h_b^{-3}}}{2} \right)^{1/2}, \tag{3.29}$$

where T_h and T_{hh} are the first and second derivatives of the temperature with respect to the film thickness, evaluated at $h = \epsilon$. Here k_c is not restricted to integer values. Changes in k_c over time result from the time dependence of the base state $h_b(t)$. When the coating liquid is nonvolatile ($\mathrm{Ca}_e = 0$) or when the coating dries uniformly [Bi = 0 in Eq. (3.3)], Eq. (3.29) reduces to the

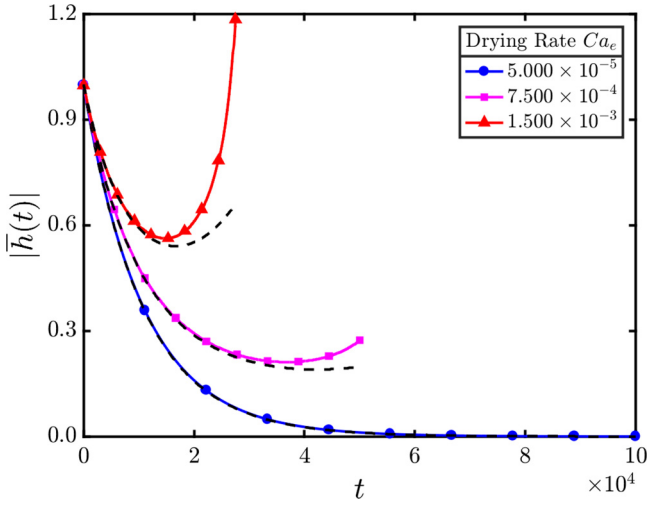

FIG. 4. Amplification magnitude $|\bar{h}(t)|$ at $k = 8$ above $k_c(t = 0) = 7.15$, 7.24, and 7.33 (in order of increasing drying rate) for We $= 50$. Colored solid lines are simulation results and black dashed lines are LSA predictions from Eq. (3.20).

expression obtained in Ref. [11]. Even for a volatile liquid ($\mathrm{Ca}_e \neq 0$), Eq. (3.29) still reduces to the expression in Ref. [11] if the coating dries uniformly, indicating that nonuniform drying [Bi $\neq 0$ in Eq. (3.3)] is necessary to shift k_c. In Fig. 2(a) the drying rate is relatively low, so k_c is approximately constant. In Fig. 2(b) the higher drying rate produces an increase in k_c as time progresses. Both of these observations are consistent with Eq. (3.29).

To further illustrate how the change in the cutoff wave number can influence film evolution, simulations of Eq. (3.1) have been carried out for a particle-free liquid for We $= 50$ and several drying rates. The initial coating is a uniform base state perturbed by a sinusoidal disturbance [Eq. (3.25)] of wave number $k = 8$, which is greater than the initial cutoff wave numbers of $k_c(t = 0) = 7.15$, 7.24, and 7.33 (in order of increasing drying rate). Initially, $\lambda_h(t)$ is negative and the amplitude of the disturbance will shrink. However, as noted above, the cutoff wave number may increase over time at elevated drying rate. Consequently, k_c is expected to surpass $k = 8$ and a local minimum in the amplification magnitude $|\bar{h}(t)|$ should be observed when the perturbation shifts from decay to growth.

To demonstrate the change in the cutoff wave number over time, the amplification magnitude $|\bar{h}(t)|$ has been determined from these simulation results as $(h_{\max} - h_{\min})/2\epsilon\alpha$ (solid lines) and compared to the LSA (dashed lines) in Fig. 4. At a low drying rate ($\mathrm{Ca}_e = 5.00 \times 10^{-5}$), the amplitude of the perturbation decreases monotonically, showing that k_c remains below $k = 8$. At elevated drying rates, local minima in $|\bar{h}(t)|$ are observed, indicating that the disturbance has shifted from decay to growth. From this we may infer that k_c has shifted over time and has surpassed $k = 8$. Practically, this increase in the cutoff wave number exposes the drying process to a wider range of instabilities. The LSA predictions agree well with the simulation results when the disturbance is decaying, but deviations appear as the disturbances begin to grow.

C. Particle-laden liquid

During drying, the colloidal particle concentration will increase as solvent is removed from the film, leading to an increase in the viscosity as described by Eq. (2.4). Additionally, increases in the initial particle concentration will raise the initial viscosity of the coating. These viscosity increases will affect the growth and decay of film-thickness perturbations. We are also interested in the fate

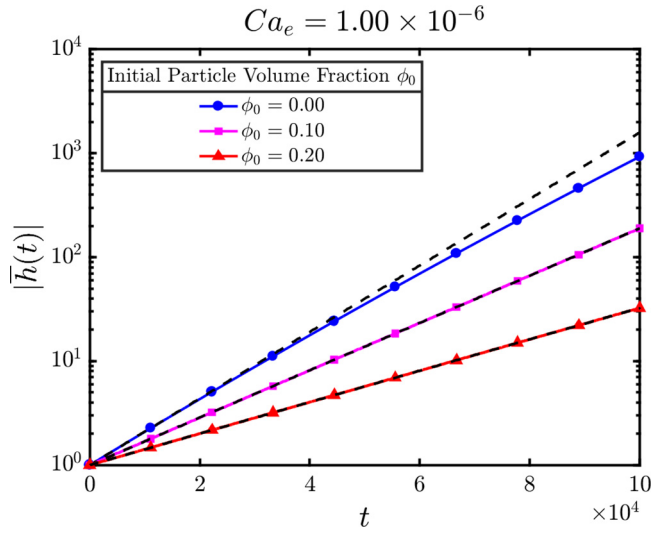

FIG. 5. Amplification magnitude $|\bar{h}(t)|$ over time at the most dangerous wave number $k_{\text{crit}} = 5$ for We $= 50$. Colored solid lines are simulation results and black dashed lines are LSA predictions from Eq. (3.22).

of compositional perturbations, which may impact the final quality of a coating [10]. Results of the LSA are compared to simulation results to explore these phenomena.

Simulations of Eqs. (3.1) and (3.2) have been performed in a rotating reference frame, as was done in Sec. III B. The initial conditions

$$h(\theta, t = 0) = \epsilon[1 + \alpha \sin(k\theta)],$$
$$\phi(\theta, t = 0) = \phi_0[1 + \alpha \sin(k\theta)] \tag{3.30}$$

are used, where k is the wave number of sinusoidal perturbations to the film thickness and particle volume fraction.

The instantaneous growth rate is given by Eq. (3.24). An increase in the particle concentration raises the viscosity, weakening the influence of surface tension and centrifugal forces. For a slowly drying film, this decrease should slow the growth or decay of the amplification magnitude $|\bar{h}(t)|$ according to Eq. (3.20).

We now explore the effects of initial particle concentration on thickness perturbations. In Fig. 5, $|\bar{h}(t)|$ has been obtained from simulations (solid lines) and the LSA (3.20) (dashed lines) at the most dangerous wave number $k_{\text{crit}} = 5$ (corresponding to We $= 50$) when We $= 50$ and $\text{Ca}_e = 1 \times 10^{-6}$. In contrast to the amplifications shown in Fig. 4, those shown in Fig. 5 correspond to $\lambda_h(t) > 0$, so $|\bar{h}(t)|$ increases monotonically over time.

As the initial particle concentration increases, the growth of perturbations is hindered by viscosity increases. For the particle-free case ($\phi_0 = 0$), the LSA results deviate from simulation results at later times as nonlinear effects are more prominent due to the faster growth. Note that although viscosity increases may be beneficial for hindering the growth of disturbances caused by centrifugal forces or evaporation, they can also hinder the leveling of disturbances by surface tension. This hindrance is undesired, as it preserves thickness variations.

We next vary the Péclet number (Pe_s) and drying rate (Ca_e) to explore the evolution of composition perturbations. In Fig. 6 the amplification magnitude $|\bar{\phi}(t)|$ from simulations (solid lines) and LSA (3.21) (dashed lines) is shown at We $= 50$ for two different drying rates and several values of Pe_s. The amplification magnitude is obtained from the simulations as $(\phi_{\max} - \phi_{\min})/2\phi_0\alpha$, where $\phi_{\max}$ and $\phi_{\min}$ are the maximum and minimum values of the particle volume fraction at a given time. The wave number chosen for these simulations is $k = 5$, the most dangerous wave number for the

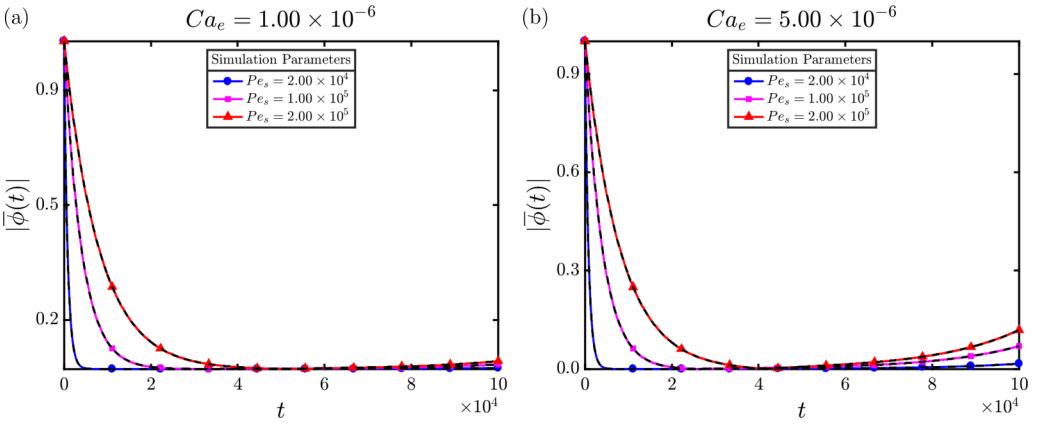

FIG. 6. Amplification magnitude $|\bar{\phi}(t)|$ over time at the most dangerous wave number $k_{\text{crit}} = 5$ for We $= 50$ and $\phi_0 = 0.10$ at (a) $\text{Ca}_e = 1.00\times10^{-6}$ and (b) $\text{Ca}_e = 1.00\times10^{-5}$. Colored solid lines are simulation results and black dashed lines are the LSA predictions from Eq. (3.21).

film thickness perturbation at We $= 50$. Thickness perturbations grow monotonically for this pair of We and k, as shown in Fig. 5. In contrast, composition perturbations as measured by $|\bar{\phi}(t)|$ evolve nonmonotonically. As can be seen in Fig. 6, there is excellent agreement between the simulation results and the LSA predictions.

At early times ($t < 5\times10^4$) in Figs. 6(a) and 6(b), diffusion of the particles causes the composition disturbance to decay quickly. For both drying rates, decay of $|\bar{\phi}(t)|$ is slowed by increasing the Péclet number, which weakens particle diffusion. Near $t = 5\times10^4$, diffusion has led to nearly complete decay of $|\bar{\phi}(t)|$ at all Péclet numbers. At later times ($t > 5\times10^4$), the composition disturbance reemerges due to growth of the thickness variations (Fig. 5, $\phi_0 = 0.10$) through the dependence of $d\bar{\phi}/dt$ on $\bar{h}(t)$ [Eq. (3.19)].

While an increase in Ca_e is expected to amplify these thickness-induced composition variations, diffusion of the particles will compete to smooth out composition variations. At $t = 1\times10^5$ in Fig. 6(b), the disturbance magnitude $|\bar{\phi}(t)|$ nearly doubles for an order-of-magnitude increase in the Péclet number. By lowering the drying rate to 1.00×10^{-6} in Fig. 6(a), drying is slowed with respect to particle diffusion, and changes in $|\bar{\phi}(t)|$ at $t = 1\times10^5$ with Péclet number become significantly smaller. The results of Fig. 6 suggest that composition gradients that form prior to drying are quickly smoothed out by diffusion, but may regrow during the later stages of drying due to film-thickness variations. In practical applications, the drying rate would be chosen so that both composition and thickness variations are within a desired tolerance.

IV. GRAVITY EFFECTS

To examine the effects of gravity, simulations of Eqs. (2.22) and (2.23) are conducted for a range of rotation rates, drying rates, and initial particle concentrations. Due to computational limitations, we set the Bond number (Bo $= 100$), Biot number (Bi $= 1.8\times10^6$), solvent viscosity ($M = 0.007$), and Péclet number (Pe $= 1\times10^6$). Moderate changes in Bo may alter the shape of the coating and affect the timescale of phenomena such as rotating-lobe decay [16], but we expect the qualitative behavior of the drying coating to remain the same. Changes in the solvent viscosity M are expected to alter the value of the critical rotation rate [Eq. (1.1)], as mentioned in Refs. [11,20]. The chosen Péclet number is representative of convection-dominated particle transport, and increases in the Péclet number are not expected to qualitatively alter the results.

For the magnitude of Bi used here, the film temperature is expected to sharply increase near the cylinder surface ($h = 0$), and a change in Bi could alter the size of this temperature gradient.

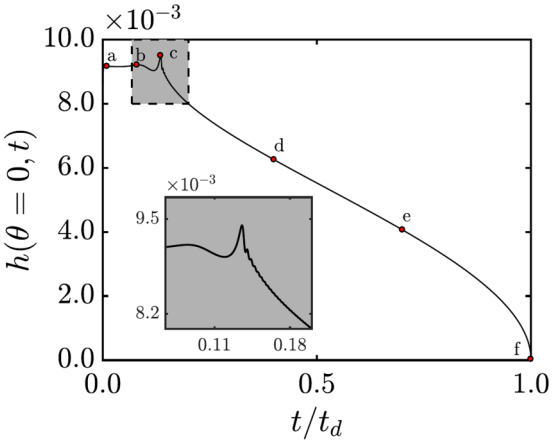

FIG. 7. Film thickness $h(\theta = 0, t)$ for $\phi_0 = 0$, $E = 1.0\times10^{-6}$, and $W = 0.012$. Time has been normalized by the dryout time for convenience. Note that during a short period near $t/t_d = 0$, $h(\theta = 0, t)$ increases from 0.007 to approximately 0.009, but this change cannot be seen on the plot.

However, because the magnitude of the latent heat of vaporization is large for most liquids, large variations in Bi do not occur for changes in the solvent. Small to moderate changes in Bi are not expected to qualitatively influence the behavior of the coating.

Since the initial viscosity varies for each particle concentration, the initial magnitude of viscous drag, controlled by $\mu(\phi_0)MW$, will vary if the five rotation rates are identical for all initial particle concentrations ϕ_0 [50]. To ensure that this drag force is comparable for different ϕ_0 at the beginning of our simulations, we set five values (0.004–0.012) of the product $\mu(\phi_0)W = W_0$ and determine the five rotation rates for each ϕ_0 by calculating $W = W_0/\mu(\phi_0)$. For each drying rate, a simulation is performed for every combination of scaled rotation rates W_0 and initial particle concentrations ϕ_0.

A. Particle-free liquid

For a nonvolatile single-component liquid, a smooth asymmetric coating may be supported on a rotating cylinder above a critical dimensionless rotation rate [13],

$$W_c = \frac{2.001\epsilon^2}{M}, \tag{4.1}$$

obtained by balancing viscous and gravitational forces in the absence of surface tension. By including surface tension, a ridge of liquid may be supported on the underside of the cylinder for $W < W_c$. Above the critical rotation rate W_c, this ridge is dragged around the cylinder as a rotating lobe that decays over time, yielding a smooth asymmetric coating after many revolutions [11]. To be consistent with terminology used in prior work, we refer to the ridge of liquid supported on the underside of the cylinder as a hanging droplet. As noted earlier, incorporating curvature in the axial direction may lead to qualitatively different results.

Figure 7 displays the time evolution of the film thickness at $\theta = 0$ for a volatile particle-free liquid ($\phi_0 = 0$) and a typical set of parameters. The rotation rate W is initially below the critical rotation rate ($W_c \approx 0.014$), so a hanging droplet is expected to form on the underside of the cylinder at early times. At early times in Fig. 7, a plateau in $h(\theta = 0, t)$ occurs, followed by a peak in $h(\theta = 0, t)$. The peak corresponds to the movement of a hanging droplet past $\theta = 0$ and the transition of this hanging droplet to a rotating lobe [11]. The gray inset in the lower left corner of Fig. 7 shows an enlargement of the main figure near the peak in thickness. Oscillations in the thickness at $\theta = 0$ (inset, Fig. 7) indicate that a liquid lobe is translating around the cylinder. The

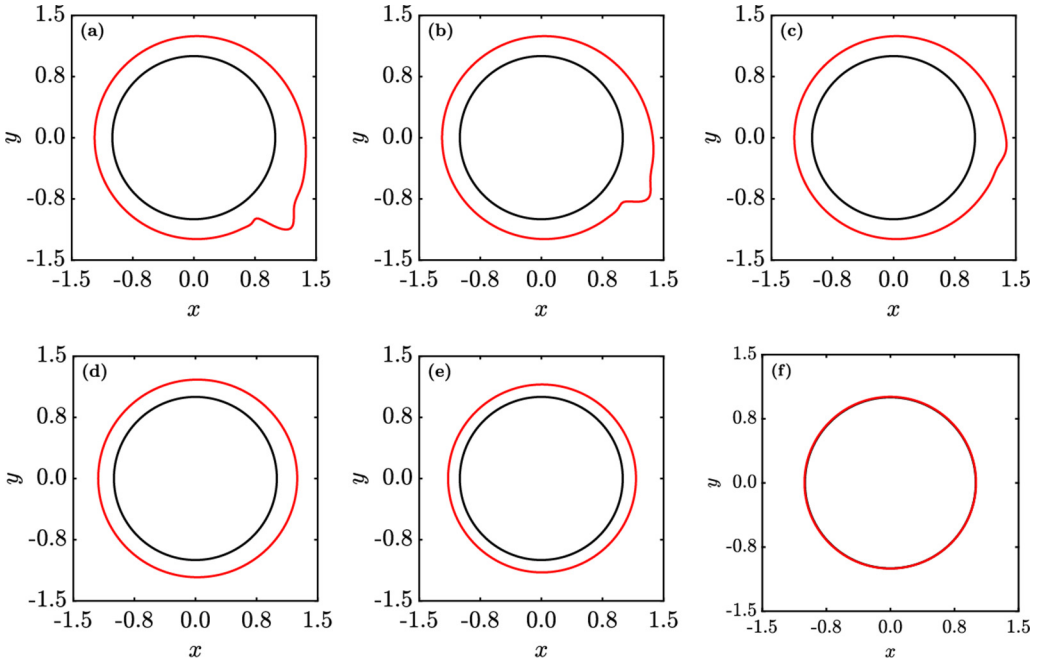

FIG. 8. Free-surface profiles of a particle-free coating at times and conditions shown in Fig. 7.

amplitude of these oscillations decreases over time, reflecting decay of the rotating lobe. For later times in Fig. 7, the rotating lobe has decayed sufficiently that oscillations are not observed.

To better illustrate the evolution of the free surface during drying, the profile of the coating on the cylinder is shown in Cartesian coordinates in Fig. 8 at time points labeled a–f from Fig. 7. At an early time [Fig. 8(a)], a hanging droplet has formed on the underside of the cylinder and sits a short distance up the side of the cylinder. As the coating dries, one might expect the thickness around the whole cylinder to decrease. Instead, the thickness remains roughly constant outside of the droplet while the droplet decreases in size [Figs. 8(b) and 8(c)], indicating that liquid is being dragged out of the droplet to replenish the mass lost in other regions of the coating.

In Fig. 8(c) the free-surface profile is shown at the peak in the thickness observed at label c in Fig. 7. This point divides the early hanging-droplet phase, where liquid is redistributed by dragging liquid from the droplet, to a late rotating-lobe phase, where redistribution of liquid occurs via motion of the droplet around the cylinder. Figures 8(d) and 8(e) show the coating profiles following decay of the rotating lobe. The coatings are reminiscent of Moffatt-type steady coating profiles [Figs. 8(d) and 8(e)], where the thickness is larger on the upward-moving side of the cylinder and smaller on the downward-moving side of the cylinder [13]. In Fig. 8(f) the minimum thickness has decreased below $\epsilon/1000$ and the simulation is ended based on our dryout criterion [Eq. (2.26)].

To examine the behavior of the coating very close to the dryout time t_d, it is useful to plot $h(\theta, t)$ versus θ/π for several times near t_d (Fig. 9). At the earliest time shown, the coating is smooth, although a slight dip in the coating thickness may be observed near $\theta/\pi = 1.0$. Over time, this trough translates toward $\theta/\pi = 1.75$ due to cylinder rotation. Since the temperature in thinner regions of the coating is higher according to Eq. (2.24), the drying rate in the trough is elevated and the depth of the trough increases over time. By $t = t_d$, the difference between the maximum and minimum thicknesses has nearly doubled as a result of this nonuniform drying, leading to rupture of the coating [cf. Eq. (2.26)]. Note that inclusion of thermal Marangoni effects would reduce the dryout time, as liquid would be driven from the thinner regions (which are warmer and have lower surface tension) to the thicker regions (which are cooler and have higher surface tension)

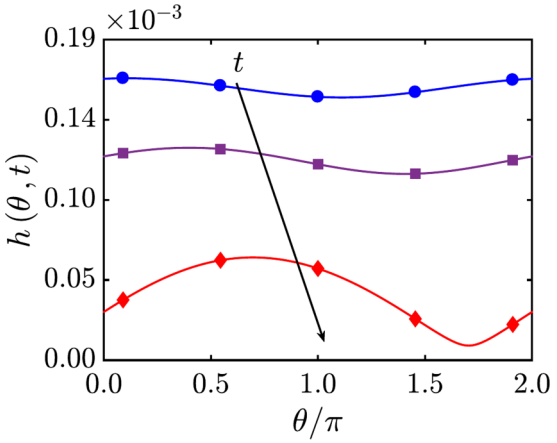

FIG. 9. Film thickness $h(\theta, t)$ very close to t_d for the parameters used in Fig. 7. From top to bottom, times are $t = 0.9995t_d$, $0.99975t_d$, and $1.0000t_d$, where $t_d \approx 4.4\times10^7$.

of the coating, as has been observed in studies of the thermocapillary effect for nonvolatile coatings [26,29].

In Fig. 10, $h(\theta = 0, t)$ versus time is shown for different rotation rates and drying rates. In Fig. 10(a), plateaus in $h(\theta = 0, t)$ may be observed at early times. During this early period, a thicker film [larger $h(\theta = 0, t)$] is supported on the upward-moving side of the cylinder at higher W due to the stronger viscous drag. Over time, drying leads to redistribution of liquid from the hanging droplet to thinner regions of the coating, causing the droplet to shrink and move closer to $\theta = 0$ [see Figs. 8(a)–8(c)]. When viscous forces fully support the hanging droplet, peaks in $h(\theta = 0, t)$ at $t/t_d \approx 0.40$, 0.30, and 0.15 (in order of increasing W) occur as the hanging droplet crosses $\theta = 0$ and transitions to a rotating lobe.

Oscillations in $h(\theta = 0, t)$ following the larger peaks indicate that a liquid lobe is translating around the cylinder. The amplitude of these oscillations decays more slowly for lower W based

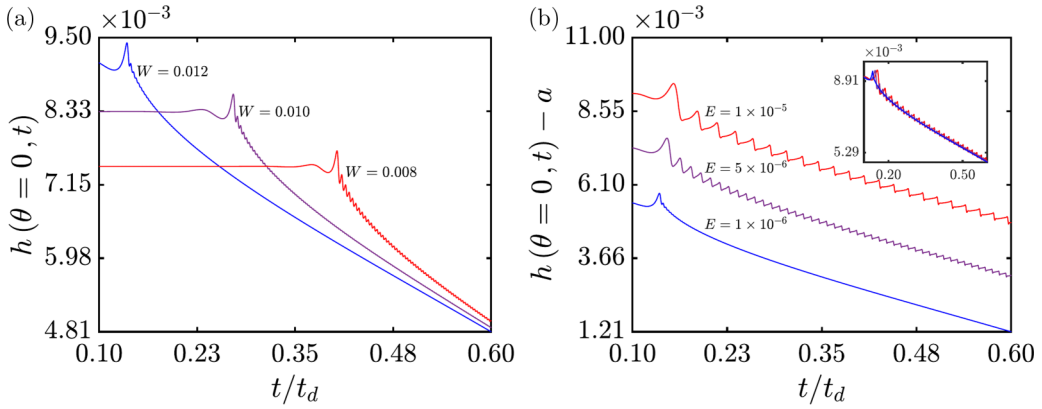

FIG. 10. Film thickness $h(\theta = 0, t)$ for a particle-free coating when (a) $E = 1.0\times10^{-6}$ and $W = 0.008$, 0.010, and 0.012 and (b) $W = 0.012$ and $E = 1.0\times10^{-6}$, 5×10^{-6}, and 1.0×10^{-5}. In (b) the three curves are offset by $a = 0$, $a = 1.8\times10^{-3}$, and $a = 3.2\times10^{-3}$ in order of descending drying rate to help distinguish between the three data sets. The same plot without an offset is included as an inset in (b). For each curve, the time has been normalized by the respective dryout time for convenience. Dryout times t_d are given in caption of Fig. 11.

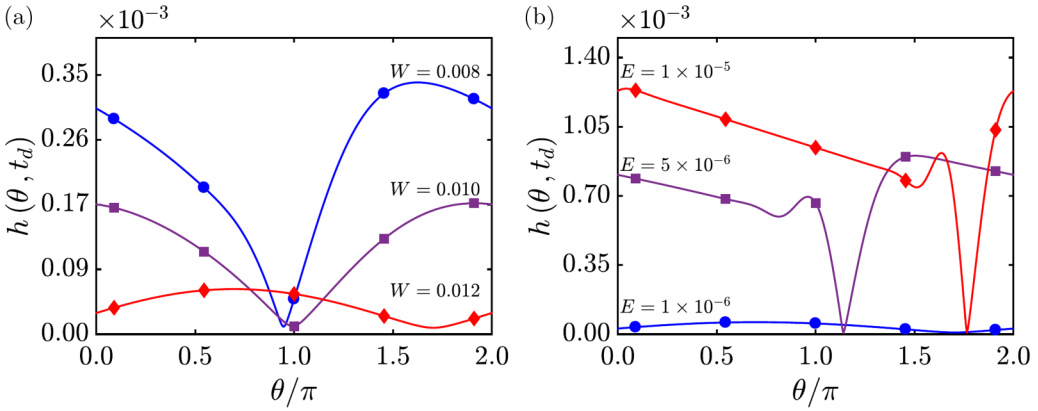

FIG. 11. Film thickness $h(\theta, t)$ versus θ/π at $t = t_d$ for the parameters shown in Fig. 10. Dryout times t_d are (a) $t_d = 4.24\times10^7$, 4.35×10^7, and 4.4×10^7 in order of increasing rotation rate W and (b) $t_d = 4.4\times10^7$, 8.7×10^6, and 4.3×10^6 in order of increasing drying rate E. Film rupture is exacerbated by higher drying rates and lower rotation rates.

on the difference in oscillation amplitudes observed for varying W. The pronounced oscillations at lower W may be ascribed to the phenomena investigated by Hinch and Kelmanson [16], who showed that decay of the rotating lobe is proportional to large powers of the coating thickness (h^3 and h^7). This can be understood by recognizing that thinner films provide more viscous resistance to flows that remove liquid from the lobe. The thickness near the transition from hanging droplet to rotating lobe decreases as the rotation rate decreases, leading to the slower decay of the rotating lobe in accordance with Ref. [16]. At later times following the peaks, larger thicknesses are observed for lower W, as weaker viscous drag leads to poorer redistribution of liquid from the upward-moving side to the downward-moving side of the cylinder. A combination of the slow lobe decay and the weaker viscous drag at low W are expected to negatively impact coating uniformity near $t = t_d$.

In Fig. 10(b), $h(\theta = 0, t)$ versus time is shown for $W = 0.012$ and three drying rates. Overlap between the results, shown in the inset in Fig. 10(b), makes them difficult to distinguish from one another, so the thicknesses have been offset by values shown in the figure caption. Evolution of these coatings occurs in a manner similar to those in Figs. 7 and 10(a), where a early hanging-droplet phase and a later rotating-lobe phase are separated by a peak in $h(\theta = 0, t)$. We focus on the oscillations in $h(\theta = 0, t)$, which are of a larger amplitude at elevated drying rates. In addition, fewer revolutions of the rotating lobe occur at higher drying rates, indicated by the spacing between oscillations. These features are a consequence of higher drying rates, which cause the film to thin faster, making it more difficult to redistribute liquid effectively before dryout occurs.

Slow decay of the rotating lobe at lower W and higher E causes coating nonuniformities to be preserved until the end of drying. Film thicknesses at dryout $h(\theta, t = t_d)$ versus the angular coordinate θ are shown in Fig. 11(a) at fixed drying rate and several rotation rates and in Fig. 11(b) at fixed rotation rate and several drying rates. Decreases in the rotation rate [Fig. 11(a)] and increases in the drying rate [Fig. 11(b)] lead to less uniform coatings, indicated by increases in thickness variations in Fig. 11. These increases occur since lower rotation rates and higher drying rates make liquid redistribution around the cylinder more difficult. The large thickness variations indicate that drying is highly nonuniform, since thinner regions dry more quickly.

B. Particle-laden liquid

In the absence of drying, Hinch and Kelmanson showed that the decay rate of the rotating lobe is inversely proportional to the liquid viscosity [16]. Increases in the initial particle concentration ϕ_0 will increase the viscosity according to Eq. (2.4) and will slow down the decay of the rotating lobe

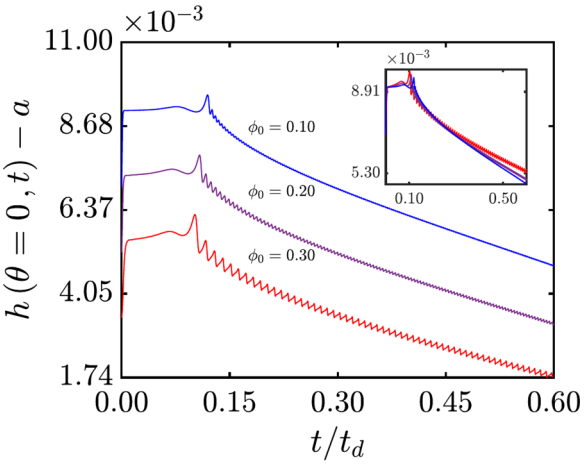

FIG. 12. Evolution of $h(\theta = 0, t)$ for a scaled rotation rate $\mu(\phi_0)W = 0.012$ and drying rate $E = 1.0\times10^{-6}$ with initial particle concentrations $\phi_0 = 0.10$, 0.20, and 0.30. Time has been normalized by the dryout times, which are $t_d = 4.3\times10^7$, 4.0×10^7, and 3.4×10^7 in order of increasing ϕ_0. The results are offset by $a = 0$, $a = 1.8\times10^{-3}$, and $a = 3.6\times10^{-3}$ in order of increasing concentration for easier comparison. The inset depicts the simulation results without an offset.

[16]. In Fig. 12, $h(\theta = 0, t)$ versus t/t_d is shown for several initial concentrations ϕ_0 at fixed drying (E) and rotation [$\mu(\phi_0)W$] rates. The results for different concentrations are offset to facilitate comparison of the data while the inset in Fig. 12 depicts the results without an offset.

An increase in the initial particle concentration from $\phi_0 = 0.10$ to $\phi_0 = 0.30$ clearly hinders decay of the lobe, as expected. Oscillations in $h(\theta = 0, t)$ are of a larger amplitude and are preserved over longer times at higher concentrations where the coating viscosity is higher. Preservation of these oscillations causes thickness variations to be maintained until dryout, at which point they are expected to grow due to nonuniform drying (see Fig. 11). In addition, viscosity increases accompanying increases in the initial particle concentration are expected to hinder liquid redistribution by slowing the leveling of thickness variations, negatively impacting final coating uniformity.

When considering the evolution of a particle-laden liquid ($\phi_0 \neq 0$), variations in the coating composition will develop which are absent in a particle-free liquid ($\phi_0 = 0$). We now explore the evolution of coating composition for a representative set of parameters and identify important features of the results. In Fig. 13, the difference between the maximum and minimum concentrations $\Delta\phi = \phi_{\max} - \phi_{\min}$ is shown versus time. The shaded inset in the center of Fig. 13 is an enlarged version of the shaded region near $t/t_d \approx 0.60$.

Oscillations in $\Delta\phi$ are a conspicuous feature in Fig. 13, as they appear, decay, and reemerge over the course drying. To explain this behavior, $h(\theta, t)$ and $\phi(\theta, t)$ are shown in Fig. 14 at the times labeled a–f in Fig. 13. Thicknesses $h(\theta, t)$ are shown by the solid, black lines and compositions $\phi(\theta, t)$ are shown by the dashed red lines. Note that the values $h(\theta, t)$ and $\phi(\theta, t)$ in the axes change for each panel. By studying the evolution of the coating thickness and composition, we will explain the evolution of $\Delta\phi$.

Figures 14(a)–14(c) show the progression of thickness and composition at the points labeled a–c in Fig. 13. A peak in the composition is observed near $\theta/\pi = 0.50$ in Fig. 14(a). This concentration peak translates through the thinnest region of the coating in Fig. 14(b) and begins translating into the thicker portion of the coating in Fig. 14(c). As we progress from Figs. 14(a) to 14(c), $\Delta\phi$ transitions from a minimum to a maximum, as shown in Fig. 13.

The oscillations observed in Fig. 13 result from convection of particle-rich coating liquid through regions of varying drying rate. The interfacial temperature and drying rate are lower in thicker regions of the coating in accordance with Eq. (2.24) and cause a slower increase in particle

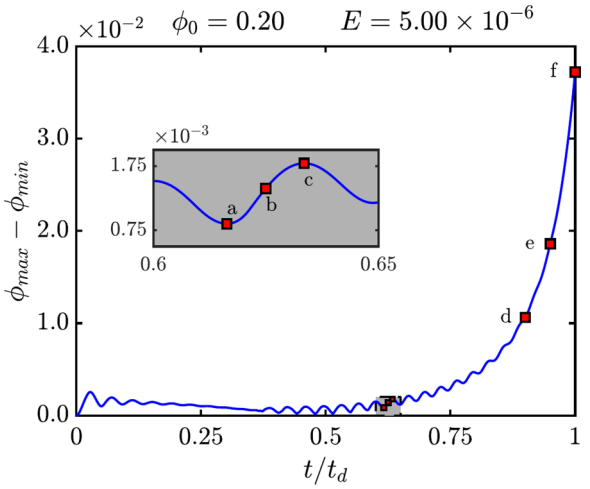

FIG. 13. Evolution of the composition variation $\Delta\phi = \phi_{\max} - \phi_{\min}$ over time for $\mu(\phi_0)W = 0.008$, $E = 5\times10^{-6}$, and $\phi_0 = 0.20$. Time has been normalized by the dryout time ($t_d = 7.7\times10^6$). The inset is a magnified image of the shaded region between $t/t_d = 0.50$ and 0.75.

concentration. As the composition peak enters the thin region of the coating, shown in Figs. 14(a) and 14(b), the drying rate is higher over the peak concentration and $\Delta\phi$ grows. As the composition peak enters the thick region of the coating, shown in Fig. 14(c), the drying rate is higher over the minimum concentration and $\Delta\phi$ shrinks. Oscillations occur as this process repeats until interrupted near t_d.

As t approaches t_d, $\Delta\phi$ grows quickly over time as shown in Fig. 13. In Figs. 14(d)–14(f), the thickness and composition are shown at points labeled d–f in Fig. 13. A steep bump in the thickness near $\theta/\pi = 1.0$ is what remains of the rotating liquid lobe [Fig. 14(d)], and we refer to the thickness peak as the location of the lobe for convenience. A peak in the particle concentration follows just

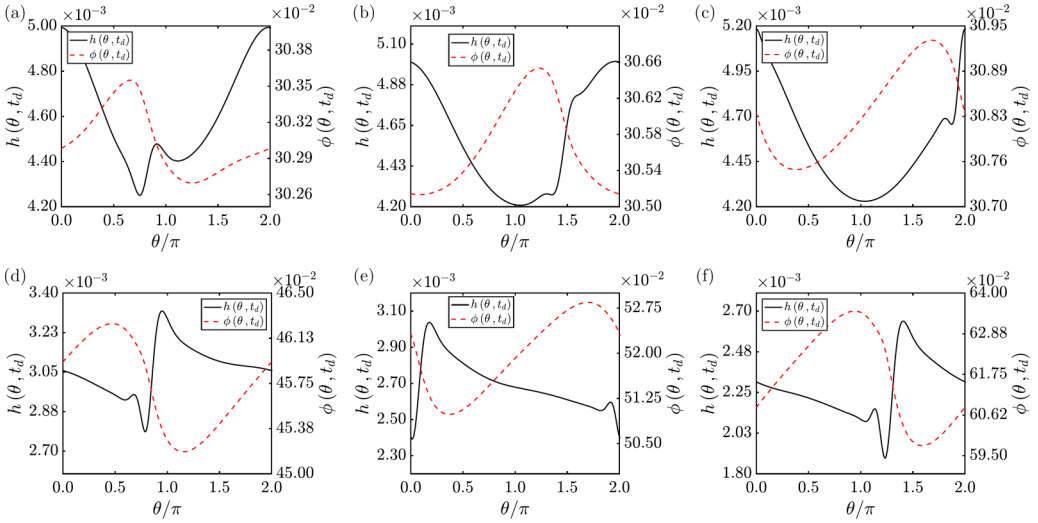

FIG. 14. Film thicknesses $h(\theta, t)$ and particle concentrations $\phi(\theta, t)$ at the times and conditions shown in Fig. 13.

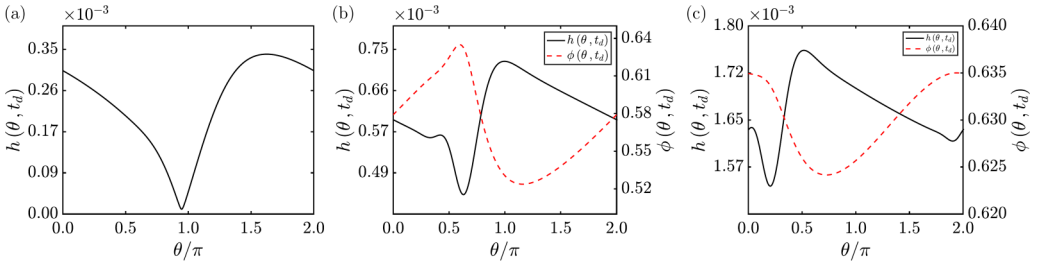

FIG. 15. Film thickness $h(\theta, t)$ and particle concentrations $\phi(\theta, t)$ at $t = t_d$ for $\mu(\phi_0)W = 0.008$ and $E = 1\times10^{-6}$. Initial particle concentrations and dryout times are (a) $\phi_0 = 0.00$ and $t_d = 4.23\times10^7$, (b) $\phi_0 = 0.05$ and $t_d = 4.22\times10^7$, and (c) $\phi_0 = 0.15$ and $t_d = 4.04\times10^7$.

behind the rotating lobe in a thin region of the coating, where the drying rate is locally higher. The minimum in particle concentration remains in the thicker region just in front of the rotating lobe, where the drying rate is lower. This results in the rapid increase in $\Delta\phi$ observed in Fig. 13, as drying is faster where the particles are already most highly concentrated [in the thinnest region [Figs. 14(d) and 14(e)]. Eventually [Fig. 14(f)], the maximum particle concentration $\phi_{\max}$ reaches the maximum allowed value and the simulation is ended.

As as result of nonuniform drying, rupture of the thinnest region of the coating occurred in the particle-free case, as shown in Fig. 9. This film rupture may be affected by the presence of particles, since solidification ($\phi_{\max} \geqslant 0.635$) could occur prior to film rupture ($h_{\min} \leqslant \epsilon/1000$). In Fig. 15 the thickness of three coatings with initial particle concentrations $\phi_0 = 0$, 0.05, and 0.15 is shown at $t = t_d$ to demonstrate the effect of particles on film rupture.

From Figs. 15(a) to 15(c), the difference $h_{\max} - h_{\min}$ decreases from 0.35×10^{-3} to 0.25×10^{-3}, demonstrating that increases in ϕ_0 hinder rupture of the coating. Instead, the particle concentration in the thinnest region of the coating approaches the maximum allowed value before rupture occurs. Additionally, an increase in ϕ_0 leads to a more uniform coating composition, which is observed by comparing Figs. 15(b) and 15(c). This is an unexpected consequence of hindering film rupture, which caused $\Delta\phi$ to increase quickly in Fig. 13. By mitigating film rupture, increases in the initial particle concentration will enhance coating thickness uniformity. Practically, this benefit will compete with the particles' negative impact on lobe decay (Fig. 12). In the following section we explore the impact of this and other factors on coating uniformity.

C. Final coating uniformity

In Fig. 16 a contour plot of the composition variation $\Delta\phi$ is shown at $t = t_d$ versus the scaled rotation rate $\mu(\phi_0)W$ and initial particle volume percent $\phi_0\times100$. Figures 16(a)–16(c) depict the

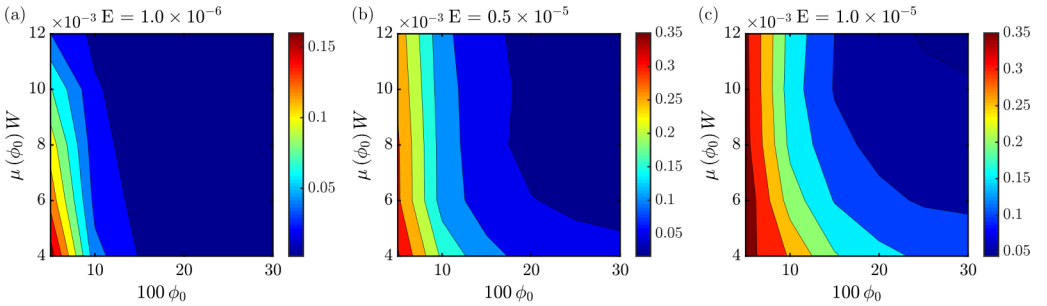

FIG. 16. Final composition variation $\Delta\phi = \phi_{\max} - \phi_{\min}$ for various scaled rotation rates $\mu(\phi_0)W$ and initial particle volume percents $\phi_0\times100$.

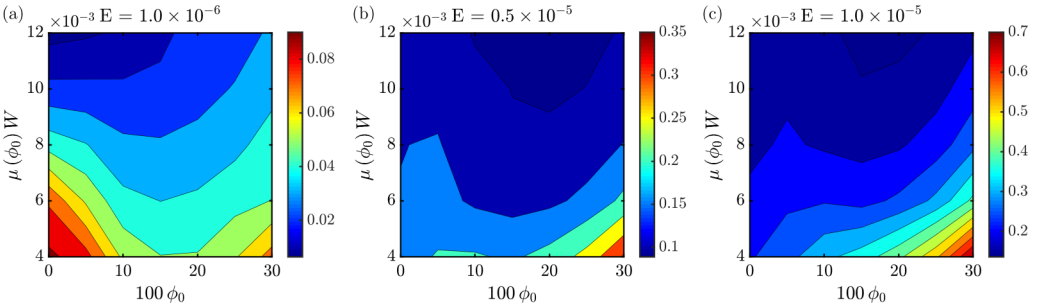

FIG. 17. Final film thickness variation $\Delta h = (h_{\max} - h_{\min})/\epsilon$ for various scaled rotation rates $\mu(\phi_0)W$ and initial particle volume percents $\phi_0 \times 100$.

results for the three drying rates $E = 1.0\times10^{-6}$, 5.0×10^{-6}, and 1.0×10^{-5}. For all three drying rates, variations in coating composition grow with a decrease in rotation rate at a fixed particle concentration, as would be expected. Decreases in the rotation rate make liquid redistribution more difficult and promote nonuniform drying near $t = t_d$ [see Sec. IV A, Figs. 10(a) and 11(a)]. As demonstrated in Figs. 13 and 14, these thickness variations and nonuniform drying cause the particle concentration to increase disproportionately in thinner regions of the coating, giving rise to composition variations. The thickness variations and nonuniform drying observed at lower rotation rates are exacerbated by increases in E, resulting in an increase in the composition variation from $\Delta\phi \approx 0.15$ to $\Delta\phi \approx 0.35$ (color bars in Fig. 16).

Additionally, composition variations shrink with an increase in initial particle concentration at a fixed rotation rate, as shown in Figs. 16(a)–16(c). It has been shown that at fixed rotation rate, an increase in the initial particle concentration hinders film rupture near $t = t_d$ by promoting solidification in thin areas, preventing deep troughs from forming in the coating thickness (Fig. 15). At the same time, solidification occurs before large variations in the particle concentration may form, causing a decrease in final composition variation with increasing initial particle concentration (Fig. 16). For higher E [Figs. 16(b) and 16(c)], viscosity increases occur more rapidly. This hinders leveling of thickness variations and causes larger composition variations at moderate rotation rates compared to what is seen at lower E [Fig. 16(a)].

In Fig. 17 a contour plot of the normalized thickness variation $(h_{\max} - h_{\min})/\epsilon$ is shown at $t = t_d$ versus the scaled rotation rate $\mu(\phi_0)W$ and initial particle volume percent $\phi_0 \times 100$. Figures 17(a)–17(c) depict the results for the three drying rates $E = 1.0\times10^{-6}$, 5.0×10^{-6}, and 1.0×10^{-5}. In general, lower drying rates E, moderate initial particle concentrations ϕ_0, and higher rotation rates $\mu(\phi_0)W$ lead to more uniform coating thicknesses. Higher rotation rates are preferable, as increases in $\mu(\phi_0)W$ smooth thickness variations [Fig. 10(a)] and mitigate rupture in thin spots on the coating [Fig. 11(a)]. Although lower drying rates tend to give more uniform thicknesses, higher drying rates may be more desirable in practical applications since this corresponds to faster solidification. In this case, Fig. 17 suggests that using higher initial particle concentrations may help minimize variations in the coating thickness. However, if the initial particle concentration is too high, liquid redistribution will be hindered by the higher viscosities and thickness variations will increase.

V. CONCLUSION

Liquid flow on the outside of a rotating cylinder serves as a model problem for studying the coating of nonflat discrete objects. After a liquid coating is applied, drying is needed to create a solidified film. The present work focuses on this drying step and thereby provides an important extension to prior work on the rotating-cylinder problem. Our study also extends prior work concerning volatile liquids on planar substrates to account for the effects of substrate curvature and rotation.

In the absence of solvent evaporation, it often useful to characterize the steady shape of a liquid film on a rotating cylinder. However, when evaporation is present, the problem becomes inherently transient. Our results show that while particle concentration gradients may initially dissipate due to diffusion, they may regrow during the later stages of drying if the evaporation rate is high enough due to nonuniform drying brought about by film-thickness variations.

When gravitational effects are significant, cylinder rotation tends to redistribute liquid around the cylinder to compensate for liquid removal via solvent evaporation. Higher evaporation rates and initial particle concentrations make this redistribution more difficult due to the increase in viscous resistance. Lower rotation rates are undesirable as well as they correspond to weaker viscous drag. However, higher particle concentrations also hinder film rupture. As a consequence of all these factors, both film thickness and composition variations are minimized at high rotation rate, low drying rate, and moderate initial particle concentration.

In practical applications, objects to be coated will be three dimensional and may have noncircular cross sections [51–53]. Curvature of the coating in the axial direction or variations in object curvature will alter the shape of the coating in the angular direction and may lead to significant changes in the results. In addition, concentration variations may arise along the depth of the film which could alter the behavior of the coating [54,55]. While lubrication-theory-based models may be used to study such depthwise concentration variations, they may not capture key features of the fluid flow such as recirculation regions, which could influence heat and mass transfer during drying [52]. Finite-element methods, both custom and commercial, are capable of handling these situations and providing insight into the limits of applicability of the lubrication approximation. While accounting for these factors will greatly change the details of the results reported here, our observations regarding liquid redistribution and the factors controlling coating uniformity are expected to be rather general and to apply to these more complicated situations as well.

ACKNOWLEDGMENTS

This work was supported by the Industrial Partnership for Research in Interfacial and Materials Engineering of the University of Minnesota. We are grateful to the Minnesota Supercomputing Institute at the University of Minnesota for providing computational resources.

APPENDIX: LINEAR STABILITY ANALYSIS

We begin by regrouping the terms in Eq. (3.18),

$$\frac{d\omega_h(t)}{dt} = -\mathrm{Ca}_e\{T_h + T_{hh}[h_b(t) - \epsilon]\} - ik\,\mathrm{Ca}_r + \frac{h_b^3}{3\mu_b(t)(1+h_b)}[(1+\mathrm{We})k^2 - k^4], \tag{A1}$$

where $\omega_h(t) = \ln \bar{h}(t)$. An expression for $\omega_h(t)$ can be obtained by integrating both sides of Eq. (A1) with respect to time over the interval $(0, t)$ to yield Eq. (3.22). The amplitude $\bar{h}(t)$ is obtained by taking the exponential of $\omega_h(t)$ as shown in Eq. (3.20).

From here we apply the integrating-factor method to obtain an expression for Eq. (3.21). Equation (3.19) is rewritten as

$$\frac{d\bar{\phi}(t)}{dt} + L(t)\bar{\phi}(t) = G(t), \tag{A2}$$

where the expressions $L(t)$ and $G(t)$ are

$$L(t) = p(t) + ik\,\mathrm{Ca}_r - \frac{k^2 q(t)}{\mathrm{Pe}}, \tag{A3}$$

$$G(t) = \frac{\alpha}{\beta} r(t) e^{\omega_h(t)}. \tag{A4}$$

Both sides of Eq. (A2) are multiplied by an integrating factor to yield

$$\frac{d}{dt}\left[\bar{\phi}(t)\exp\left(\int_0^t L(\zeta)d\zeta\right)\right] = G(t)\exp\left(\int_0^t L(\zeta)d\zeta\right). \tag{A5}$$

Integration of both sides of Eq. (A5) over the interval $(0, t)$ yields

$$\bar{\phi}(t)\exp\left(\int_0^t L(\zeta)d\zeta\right) - 1 = \int_0^t G(\zeta)\exp\left(\int_0^\zeta L(\xi)d\xi\right)d\zeta. \tag{A6}$$

The expression $\omega_\phi(t)$ may be defined as

$$\omega_\phi(t) = \int_0^t L(\zeta)d\zeta. \tag{A7}$$

By substituting Eqs. (A3) and (A4) into Eqs. (A6) and (A7) and solving for $\bar{\phi}(t)$ in Eq. (A6), the expressions shown in Eqs. (3.21) and (3.23) may be obtained.

[1] D. Castro, S. Wu, K. L. Woolbright, K. W. Scheinpflug, S. F. A. Hossainy, and L. Chen, Apparatus and method for depositing a coating onto a surface of a prosthesis, U.S. Patent No. 6,395,326 (28 May 2002).

[2] P. Heller, A. Heldman, J. Foehlich, and D. Kim, Method and apparatus for coating an endoprosthesis, U.S. Patent Application No. 20030215564 (pending).

[3] Y. Chen and H. Ho, System and method for coating an implantable medical device, U.S. Patent No. 7,563,324 (21 July 2009).

[4] R. A. Chappa, A. G. Bach, and M. Macgregor, Apparatus and methods for coating medical devices, U.S. Patent No. 9,623,215 (18 April 2017).

[5] S. M. Benjamin, S. M. Bennett, J. C. Bew, and J. L. Swank, Process for preparing a sugar coating on an irregular shaped confection, U.S. Patent Application No. 20080026131 (pending).

[6] D. N. Cade and D. H. Xiongwei, Hydroxypropyl methyl cellulose hard capsules and process of manufacture, U.S. Patent No. 9,655,860 (23 May 2017).

[7] A. Lee, P. T. Brun, J. Marthelot, G. Balestra, F. Gallaire, and P. M. Reis, Fabrication of slender elastic shells by the coating of curved surfaces, Nat. Commun. **7**, 11155 (2016).

[8] N. Keefer and B. Bosch, Molded fuel tank and method of manufacturing the same, U.S. Patent No. 10,023,322 (17 July 2018).

[9] N. Fujitaka and A. Kobayashi, Rotational-molded resin fuel tank, U.S. Patent Application No. 20060068139 (pending).

[10] C. M. Cardinal, Y. D. Jung, K. H. Ahn, and L. F. Francis, Drying regime maps for particulate coatings, AIChE J. **56**, 2769 (2010).

[11] P. L. Evans, L. W. Schwartz, and R. V. Roy, Steady and unsteady solutions for coating flow on a rotating horizontal cylinder: Two-dimensional theoretical and numerical modeling, Phys. Fluids **16**, 2742 (2004).

[12] P. L. Evans, L. W. Schwartz, and R. V. Roy, Three-dimensional solutions for coating flow on a rotating horizontal cylinder: Theory and experiment, Phys. Fluids **17**, 072102 (2005).

[13] H. K. Moffatt, Behaviour of a viscous film on the outer surface of a rotating cylinder, J. de Mécanique **16**, 651 (1977).

[14] M. A. Kelmanson, Theoretical and experimental analyses of the maximum-supportable fluid load on a rotating cylinder, J. Eng. Math. **29**, 271 (1995).

[15] L. Preziosi and D. D. Joseph, The run-off condition for coating and rimming flows, J. Fluid Mech. **187**, 99 (1988).

[16] E. J. Hinch and M. A. Kelmanson, On the decay and drift of free-surface perturbations in viscous thin-film flow exterior to a rotating cylinder, Proc. R. Soc. London A **459**, 1193 (2003).

[17] V. V. Pukhnachev, Motion of a liquid film on the surface of a rotating cylinder in a gravitational field, J. Appl. Mech. Tech. Phys. **18**, 344 (1977).

[18] T. P. Hynes, Stability of thin films, Ph.D. thesis, University of Cambridge, 1978.
[19] E. A. Karabut, Two regimes of liquid film flow on a rotating cylinder, J. Appl. Mech. Tech. Phys. **48**, 55 (2007).
[20] W. Li and S. Kumar, Three-dimensional surfactant-covered flows of thin liquid films on rotating cylinders, J. Fluid Mech. **844**, 61 (2018).
[21] A. v. B. Lopes, U. Thiele, and A. L. Hazel, On the multiple solutions of coating and rimming flows on rotating cylinders, J. Fluid Mech. **835**, 540 (2018).
[22] M. A. Kelmanson, On inertial effects in the Moffatt-Pukhnachov coating-flow problem, J. Fluid Mech. **633**, 327 (2009).
[23] R. V. Craster and O. K. Matar, Dynamics and stability of thin liquid films, Rev. Mod. Phys. **81**, 1131 (2009).
[24] A. Oron, S. H. Davis, and S. G. Bankoff, Long-scale evolution of thin liquid films, Rev. Mod. Phys. **69**, 931 (1997).
[25] M. H. Eres, D. E. Weidner, and L. W. Schwartz, Three-dimensional direct numerical simulation of surface-tension-gradient effects on the leveling of an evaporating multicomponent fluid, Langmuir **15**, 1859 (1999).
[26] A. Oron and P. Rosenau, Formation of patterns induced by thermocapillarity and gravity, J. Phys. II **2**, 131 (1992).
[27] T. Pham, X. Cheng, and S. Kumar, Drying of multicomponent thin films on substrates with topography, J. Polym. Sci. B **55**, 1681 (2017).
[28] T. Pham and S. Kumar, Drying of droplets of colloidal suspensions on rough substrates, Langmuir **33**, 10061 (2017).
[29] B. Reisfeld and S. G. Bankoff, Non-isothermal flow of a liquid film on a horizontal cylinder, J. Fluid Mech. **236**, 167 (1992).
[30] S. G. Yiantsios and B. G. Higgins, A mechanism of Marangoni instability in evaporating thin liquid films due to soluble surfactant, Phys. Fluids **22**, 022102 (2010).
[31] S. D. Howison, J. D. Moriarty, J. R. Ockendon, E. L. Terrill, and S. K. Wilson, A mathematical model for drying paint layers, J. Eng. Math. **32**, 377 (1997).
[32] J. P. Burelbach, S. G. Bankoff, and S. H. Davis, Nonlinear stability of evaporating/condensing liquid films, J. Fluid Mech. **195**, 463 (1988).
[33] L. Espín and S. Kumar, Sagging of evaporating droplets of colloidal suspensions on inclined substrates, Langmuir **30**, 11966 (2014).
[34] L. Espín and S. Kumar, Forced spreading of films and droplets of colloidal suspensions, J. Fluid Mech. **742**, 495 (2014).
[35] B. Tsai, M. S. Carvalho, and S. Kumar, Leveling of thin films of colloidal suspensions, J. Colloid Interface Sci. **343**, 306 (2010).
[36] K. J. Ruschak and L. E. Scriven, Rimming flow of liquid in a rotating cylinder, J. Fluid Mech. **76**, 113 (1976).
[37] S. H. Maron and P. E. Pierce, Application of Ree-Eyring generalized flow theory to suspensions of spherical particles, J. Colloid Sci. **11**, 80 (1956).
[38] I. M. Krieger and T. J. Dougherty, A mechanism for non-Newtonian flow in suspensions of rigid spheres, Trans. Soc. Rheol. **3**, 137 (1959).
[39] B. R. Duffy and S. K. Wilson, Large-Biot-number non-isothermal flow of a thin film on a stationary or rotating cylinder, Eur. Phys. J.: Spec. Top. **166**, 147 (2009).
[40] E. Boujo and M. Sellier, Pancake making and surface coating: Optimal control of a gravity-driven liquid film, Phys. Rev. Fluids **4**, 064802 (2019).
[41] J. M. Delhaye, Jump conditions and entropy sources in two-phase systems. local instant formulation, Int. J. Multiphase Flow **1**, 395 (1974).
[42] J. C. Slattery, *Interfacial Transport Phenomena*, 2nd ed. (Springer, New York, 2007).
[43] C. Sodtke, V. S. Ajaev, and P. Stephan, Dynamics of volatile liquid droplets on heated surfaces: Theory versus experiment, J. Fluid Mech. **610**, 343 (2008).

[44] R. D. Deegan, O. Bakajin, T. F. Dupont, G. Huber, S. R. Nagel, and T. A. Witten, Contact line deposits in an evaporating drop, Phys. Rev. E **62**, 756 (2000).
[45] W. Li and S. Kumar, Thin-film coating of surfactant-laden liquids on rotating cylinders, Phys. Fluids **27**, 072106 (2015).
[46] O. E. Jensen and J. B. Grotberg, The spreading of heat or soluble surfactant along a thin liquid film, Phys. Fluids A **5**, 58 (1993).
[47] L. W. Schwartz, R. V. Roy, R. R. Eley, and S. Petrash, Dewetting patterns in a drying liquid film, J. Colloid Interface Sci. **234**, 363 (2001).
[48] H. Ji and T. P. Witelski, Instability and dynamics of volatile thin films, Phys. Rev. Fluids **3**, 024001 (2018).
[49] T. A. Driscoll, N. Hale, and L. N. Trefethen, *Chebfun Guide* (Pafnuty, Oxford, 2014).
[50] C. Parrish, Ph.D. thesis, University of Minnesota (unpublished).
[51] A. K. Sahu and S. Kumar, Thin-liquid-film flow on a topographically patterned rotating cylinder, Phys. Fluids **26**, 042102 (2014).
[52] W. Li, M. S. Carvalho, and S. Kumar, Liquid-film coating on topographically patterned rotating cylinders, Phys. Rev. Fluids **2**, 024001 (2017).
[53] W. Li, M. S. Carvalho, and S. Kumar, Viscous free-surface flows on rotating elliptical cylinders, Phys. Rev. Fluids **2**, 094005 (2017).
[54] K. Maki and S. Kumar, Fast evaporation of spreading droplets of colloidal suspensions, Langmuir **27**, 11347 (2011).
[55] S. G. Yiantsios and B. G. Higgins, Marangoni flows during drying of colloidal films, Phys. Fluids **18**, 082103 (2006).